High speed in-process defect detection in metal additive manufacturing

Siwen Chen

Supervisors: Prof. Richard Leach

Dr. Simon Lawes

Faculty of Engineering

University of Nottingham

This thesis is submitted for the degree of

Master of Philosophy

March 2021

Table of Contents

1. Introduction 3

1.1 Motivation 3

1.2 Aims and objectives 3

1.3 Structure of the thesis 4

2. Literature review 6

2.1 Review of the major types of defects in AM process 6

2.1.1 Pores 7

2.1.1.1 Lack of fusion 8

2.1.1.2 Keyhole 9

2.1.1.3 Gas formed by metal vapour 11

2.1.2 Crack 11

2.1.3 Balling behaviour 15

2.1.4 Un-melted particles 16

2.1.5 Pits 17

2.1.6 Scratches 17

2.1.7 Deformation 18

2.1.8 Signatures of defects 18

2.1.8.1 Melt pool 19

2.1.8.2 Weld track 19

2.1.8.3 Surface roughness 19

2.2 Review of the popular measurement / monitoring techniques for LPBF 20

2.2.1 In-line measurement instrument structures and information sources 21

2.2.1.1 Coaxial structure / visible and infrared light information in-line detection 21

2.2.1.2 Off-axial structure / visible and infrared light information in-line detection 22

2.2.1.3 Photodiode in-line detection 23

2.2.2 Offline detection technologies 23

2.2.2.1 Micro-CT technology 23

2.2.2.2 Optical metrology instruments 24

3. Methodology 26

4. ML applications for defect detection / feature extraction in LPBF 29

4.1 ML for defect detection and prediction 29

4.1.1 Defect detection with visual data 35

4.1.2 Defect detection with multi-sensor data 35

4.2 Part inspection and validation 37

5. Measurements of AM surfaces 38

5.1 Samples 38

5.2 FV measurement setting optimisation 38

5.2.1 Utilise the correct objective lens 38

5.2.2 Select the right illumination source 39

5.2.3 Choose the optimal instrument resolution 39

5.3 Fringe projection measurement 39

6. Machine learning database preparation 42

6.1 Filtering methodologies selection and comparison 42

6.2 Data augmentation 44

7. Defect detection with the application of different types of machine learning algorithms 46

7.1 Application of PCA in feature identification 47

7.1.1 Image parameter identification 47

7.1.2 Experiment on the basis of PCA 48

7.2 Application of CNN in feature identification 50

7.2.1 Convolutional neural network architecture 50

7.2.1.1 Convolutional layer 51

7.2.1.2 Pooling layer 53

7.2.1.3 Fully-connected layer 53

7.2.2 Training process 54

7.2.3 Pre-processing 54

7.2.4 Overfitting tackling 55

7.2.5 Results of model validation based on FV dataset 55

7.2.6 Results of model validation based on fringe projection dataset 56

7.3 Application of U-Net in defect segmentation 57

7.3.1 Architecture 57

7.3.2 Model framework and parameter settings 58

7.3.3 Training optimisation 59

7.3.4 Overfitting tackling 59

7.3.5 Results of model training and validation 59

8. Discussion 63

8.1 Overview of the research methodology 63

8.2 The advantages and disadvantages of the used ML methods 64

8.2.1 PCA 64

8.2.2 CNN (MobileNet) 64

8.2.3 U-Net 65

9. Conclusions 66

9.1 Thesis summary 66

9.2 Contributions to the research field 69

9.3 Areas for future work 72

9.3.1 U-Net **Error! Bookmark not defined.**

References 73

1. Introduction

1.1 Motivation

Additive manufacturing (AM) is defined as 'the process of joining materials to make objects from 3D model data, usually layer upon layer, as opposed to subtractive manufacturing technologies' [1]. This fabricating technique is also famously known as '3D printing' [2]. The laser powder bed fusion process (LPBF), as one of the most commonly applied manufacturing technique within additive manufacturing area is a fabricating process of fusing metal or polymer materials to produce parts. After the determination of the computer-aided design (CAD) for specific purposes, the files will be transferred to the AM device, thereafter an electron beam is activated in the chamber of the AM machine, melts layers of powders in the powder bed following the designed patterns in a layer by layer manner. Initially, only the first layer will be melted progressively by the laser with high energy input, subsequently, the entire powder bed is moved downwards and a process called recoating is conducted to deposit a second layer of fine powders uniformly. The above processes will be continued until the entire parts are completely fabricated. After the manufacturing process, the chamber will be opened and those unremoved redundant, unused or un-melted powders will be removed from the powder bed.

Although the entire manufacturing chain is becoming more mature by improved pre-defined design, more accurate heat input and motion system and cleaner in-chamber atmosphere, there are still a number of influential factors that can have a negative impact on the manufacturing process that introduce 'defects', which will greatly lessen the density of the parts or even result in failure.

1.2 Aims and objectives

As defects will lead to less densified parts or even failed products in a worse case scenario, it is critical to be able to discover them effectively during the manufacturing process. So the first aim of this thesis is to develop a methodology for the measurement and characterisation of surface texture of AM parts. Typically, optical metrology instruments including focus variation (FV) microscopy and fringe projection (FP) have been used to measure the surface texture of AM samples due to their suitability and reliability in the field of metrology [3]. To

secure a high quality of measurement, these metrology techniques have various measurement settings (e.g. objective lens, illumination source, resolution) that can be adjusted. Suitable evaluations of optimised settings for the measurement of AM surfaces are needed for the corresponding measurement techniques.

The second aim of this thesis is to better process the measured results, suitable filtration methods need to be applied to characterise the surface and suppress the measurement noise. Surface filtration is a technology by which different spatial wavelength components of surface texture, which are roughness, waviness and shape error can be extracted from measurement data for further characterisation. Hence, several filtering methods need to be compared with to discover the most feasible filter.

Lastly, in the recent decades, machine learning (ML) is presenting a high robustness and applicability in defect detection in comparison to the traditional digital image processing technique. In this thesis, several ML techniques have been investigated into in terms of their suitability for the research based on the processed data secured from the optical measuring instrument.

In summary, the aims are:

1. Determine the optimum instrument settings and good practices for using the selected instrument to measure the surface topography of the AM surface.
2. Develop optimum filtration methodology to characterise the AM surface by comparing different filters.
3. Achieve defect detection (defect classification and defect segmentation) with the use of different ML methods.

1.3 Structure of the thesis

In Chapter 1, the motivation along with the aims and objectives of the thesis are presented.

In Chapter 2, a review of defects appearing in AM parts and their signatures in conjunction with a review of popular in-line measurement / metrology instruments for AM surfaces are presented to provide rich background information for the following research.

In Chapter 3, the research route throughout the thesis is presented, including the AM samples and the measurement instruments used, the preparation that needs to be done prior to the data

being used by ML and the selection of ML algorithms.

In Chapter 4, a review of the applications of different ML methods in AM, including defect detection with visual data, anomaly detection with multi-sensor data and part inspection.

In Chapter 5, a study to determine the optimised measurement settings of measuring instruments for AM parts is presented. Another purpose of this chapter is to facilitate the development of good practice for such sort of measurements.

In Chapter 6, for the purpose of facilitating the use of the measuring results in the following ML methods, the optimised filtration method is determined by comparing several filtration methods. In addition, typical ML database augmentation operation is applied to expand the size of the database to improve the performance of the learning.

In Chapter 7, different ML methods, including unsupervised learning and supervised learning are investigated into to test their suitability and defect detection capability, against the data from the measurement instruments.

In Chapter 8, the overview of the proposed methodology is given and the major advantages and disadvantages of the ML methods used in this thesis are discussed.

In Chapter 9, the conclusions of the thesis are presented in terms of how the aims and objectives of the thesis are accomplished.

2. Literature review

2.1 Review of the major types of defects in AM process

As discussed above, defects are those imperfections located in the LPBF parts which will lessen the densities of the parts, shorten the fatigue life and thus have a harmful impact on the quality of the parts. Although efforts will be made to classify them into several major types in terms of their appearances, sizes, causes and effects, the term is still used generally in many research, since 1) some defects cannot simply be categorized as a single type as they are combinations of different sorts of defects but coincidentally fuse together to form a newer defect; 2) With respect to the limitations of the measuring technologies, and the similarities of some different types of defects, it is difficult to distinguish the sort of the concerned defects and identify which type they belong to. Fig 2.1 illustrates a defect (pore) including other defects (gas bubbles, particles) [4]. Another typical example of combined defect is illustrated in Fig 2.2, which is a big gas bubble joined by two smaller ones [5].

For clarifying some concepts in the following sections, some terms are explained as follows.

1) Process signature

With regard to engineering areas, ‘signature’ is defined as ‘a distinctive pattern, product, or characteristic by which something can be identified’. According to the definition, a signature of defects is referring to the pattern or phenomenon that defects can generate.

2) Melt pool

Melt pool is a concave area where the powders have been melted by the applied laser beam and are still in the liquid status.

3) Weld track

Weld tracks are the stripes on the powder bed along the scanning direction, which form as a result of the re-consolidation of the melted material.

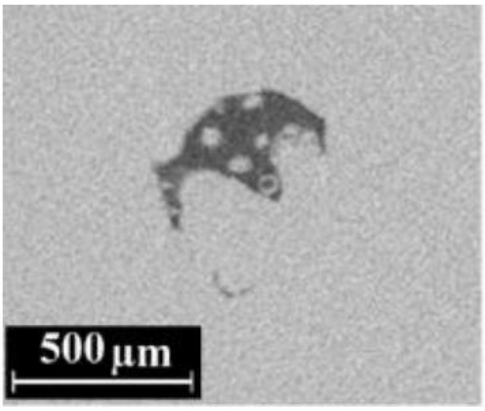

Fig 2.1 CT scanned image of combined defects in AlSi10Mg part [4] produced by LPBF

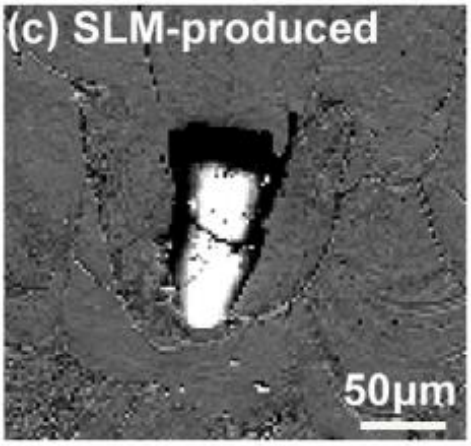

Fig 2.2 SEM image of combined defects in Ti6Al4V part [5] produced by LPBF

2.1.1 Pores

Pores, as illustrated in Fig 2.3, can be harmful to the quality of the additively manufactured parts which lessen the density of parts, act as initiation site for cracks and thus lead to failed parts. They can usually be classified as lack of fusion pores, keyhole pores, gas bubbles, according to their appearances and formation processes.

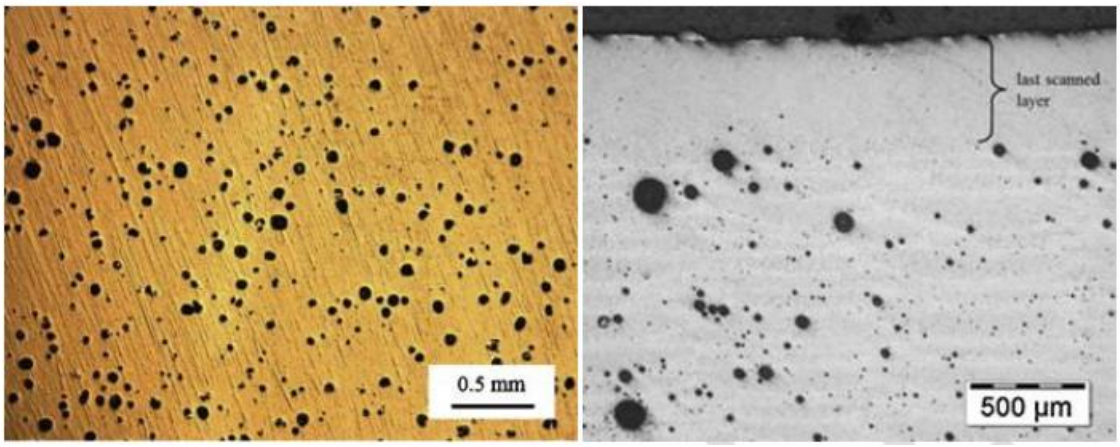

Fig 2.3 Cross section of spherical gas pores in Ti6Al4V [6] and AlSi10Mg [7] parts produced by LPBF

Pores have a variety of shapes, which are spherical, elliptical, elongated and irregular, typically, where the former two shapes usually represent gas bubbles or keyhole pores whereas the elongated, irregular shapes typically represent lack of fusion pores. The porosity in the sample can be affected by different building locations in the chamber [8]. Khairallah et al. [9] demonstrated that pores form differently at different positions on the powder bed.

Engeli et al. [10] stated that high porosity is attributed to low powder density, inappropriate local powder properties, poor recoating process and/or unstable gas flow [9,11]. Several studies have been carried out to determine the effect of the process parameters on the generation of pores. It was stated that the pore formation and its mechanism, distribution, size are attributed to scanning strategies [12], scanning speed [10], layer thickness [13,14], laser energy input [15], spot size [16] and/or hatch spacing [17].

2.1.1.1 Lack of fusion

Lack of fusion is due to the process of under-melting where the laser energy input is not sufficient to achieve complete melting, as in Fig 2.4 [18]. It could be generated at the connecting point of adjacent weld tracks without sufficient overlap and in between the discontinuities of weld tracks [19,20]. Darvish et al. [21] discovered that the sizes of most lack of fusion defects can vary from 100 μm^2 to 1375 μm^2, in which the latter one is considered abnormal. It was also reported that the elongated pores are with a size up to 50 µm by Yadroitsev [22].

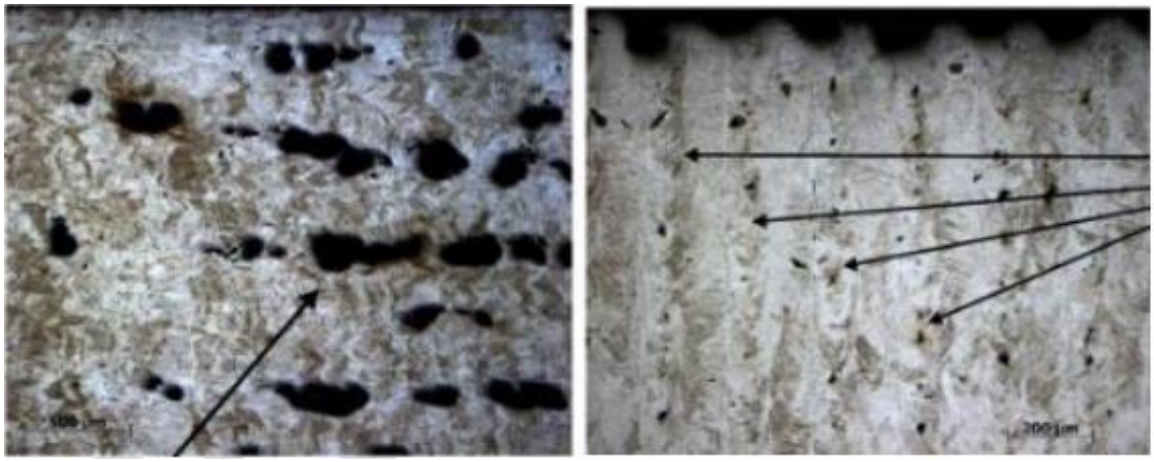

Fig 2.4 Micrographs of cross section of lack of fusion pores in Ti6Al4V part [18] produced by LPBF

Scanning strategies are mainly responsible for the generation of lack of fusion pores. Several studies showed that high scanning speed [13,21,23], insufficient laser energy input [24], great hatch spacing [25,26] and inappropriate building orientation [27] will lead to this type of pores. The poor liquid flowability and instability of the melt pool during the manufacturing process account for the formation of lack of fusion pores as well [22,24]. Also, it was stated that un-melted particles and large spatters that land on the surface will lead to large lack of fusion pores (more than 1000 μm^2) [20,28].

Miranda et al. [29] stated that the lack of fusion in the layers is the major cause for the low material density. They stated that the lack of fusion pores with a typical size of 500 μm would lead to lower consolidation and thus lower density. It was also stated that the lack of fusion pores with such size will worsen the layer bonding condition [19]. Darvish et al. [21] suggested that the lack of fusion pores ought to be less than 1375 μm^2 (dimension = $\sqrt{area}$ < 37 μm) in order to secure a highly densified structure and remove abnormal lack of fusion pores. The majority of the defects Kobryn et al. [30] and Cottam et al. [31] found are the defects caused by lack of fusion, primarily forming between and being parallel to the layers or pores.

2.1.1.2 Keyhole

Keyhole pores are caused by depression cavity collapse [32] and are termed as such because of their shape, as shown in Fig 2.5. They can be typically characterised with a wider upper top and sharp angle structure at the bottom [22], and they appeared to be located in the areas

distant to the top surface and at bottom of melt pool [22,30].

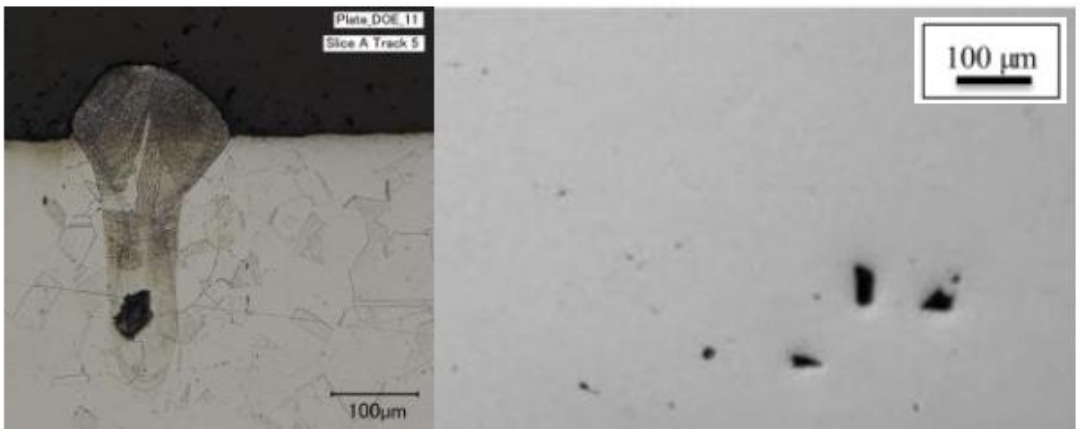

Fig 2.5 SEM images of cross sections of keyhole pores in 316L [33] and AISI SS 440 parts [16] produced by LPBF

Keyhole pores could be caused by the entrapped gas bubbles in the layers while the laser energy input is high [31,34-37]. Related studies also revealed that the formation of keyhole pores is caused by the vaporization of the materials which have lower melting point within the alloy [22,30]. The instability of the melt pool, which is caused by Marangoni and recoil forces in the melt pool, will result in the formation of keyhole pores too [31,32,38,39,40-42]. Particularly, keyhole pores are more likely to be formed while the melting material has a high rate of flow in the melt pool [34]. In addition, the melt pool will even collapse when its instability increases significantly. As a result, keyhole pores will form [19].

Liu et al. [17] suggested that the formation of a keyhole pore usually yields the undesirable large melt zone depth and thus increases the risk of layer collapse. Also, it was suggested that the collapse of keyhole pores accounts for the un-melted particles in the denudation zone and subsequent pore formation [37]. Fig 2.6 indicates that the keyhole pores that will cause melt pool collapse and therefore result in severely coarse layers are spherical, with size of 25 μm, locating at the end of weld tracks, as shown in the top view of the surface under SEM. In addition, it can be visualized in Fig 2.6 the un-melted particles with similar size to such keyhole pores will also be responsible for the high surface roughness.

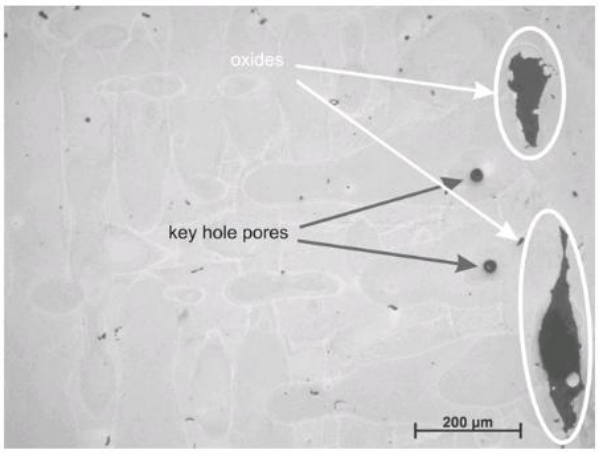

Fig 2.6 SEM image of keyhole pores and particles observed on the surface from a top view of AlSi10Mg part produced by LPBF [36]

2.1.1.3 Gas formed by metal vapour

Gas bubbles are also a specific type of pores, which are entrapped within the samples. The formation of gas bubbles is because of 1) the evaporation of the different sorts of metal materials with relatively low melting point inside the local powders; 2) the inherent porosity in new powders. Both types of the gases have a spherical shape and are less than 50 μm, typically.

Weingarten et al. [7] stated that gas pores can usually be characterized by spherical shape. It was stated that the pores can form in between adjacent layers and at the front of the weld tracks [6,17], with a size ranging from 10 μm to 50 μm and be spherical shaped [43]. However, in particular, based on the research of Liu et al. [44], the gas bubbles generated due to tin vaporization are usually with a conical shape.

Several studies demonstrated that scanning strategy usually affects the formation of gas pores, including smaller laser spot size [45], increase in the laser energy input [25], and low scanning speed [46]. As tin has the lowest boiling point among the metal materials in the powders, tin vaporization can form gas bubbles in the manufacturing process as well [45]. Anisimov et al. [47] reported 18% of the vapour would condense and fall back to the surface during the re-consolidation process and hence form gas bubbles.

2.1.2 Crack

Crack phenomenon is one of the most significant types of defects that will yield the failure of additively manufactured parts. It can be termed as “a fracture type discontinuity characterised

by a sharp tip and high ratio of length and width" [47]. A typical crack usually includes minor fracture surfaces or complex structures [4,48], including rough cup-cone features (Fig 2.7), terrace-like features (Fig 2.8) [49] and ductile dimple features. It was discovered that the surface of the cracks in the areas of pores is relatively smooth [8,9,41,50]. Researchers have also been paying attention to the locations of the initiation or propagation sites of cracks. They demonstrated that the crack initiates mainly on the fracture surface or the subsurface [4,51-53], middle and outer regions of the AM surface [16,54,55], and areas that are filled with un-melted particles and large defects [45]. Kasperovich et al. [56] found that the small fractures in the parts are typically with a size of 10's of μm.

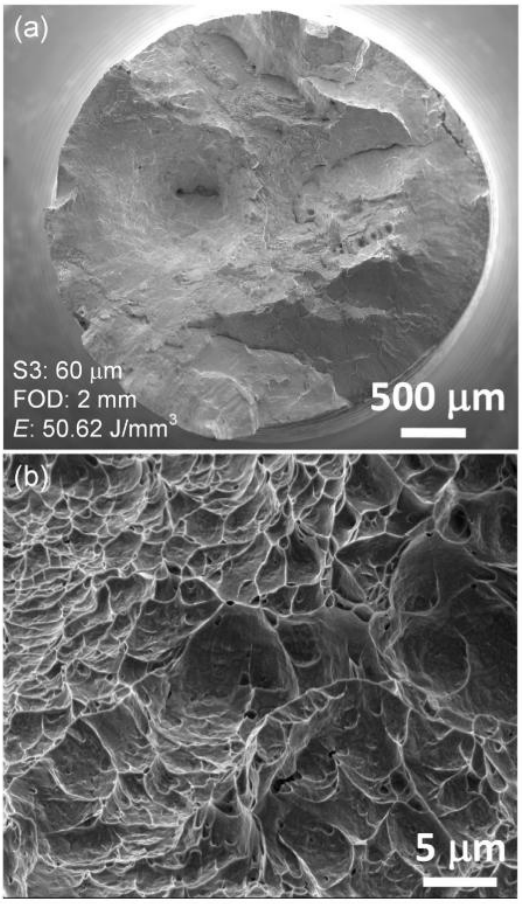

Fig 2.7 (a) SEM images of cup-cone structure factures and (b) dimple fractures in Ti6Al4V part produced by LPBF [49]

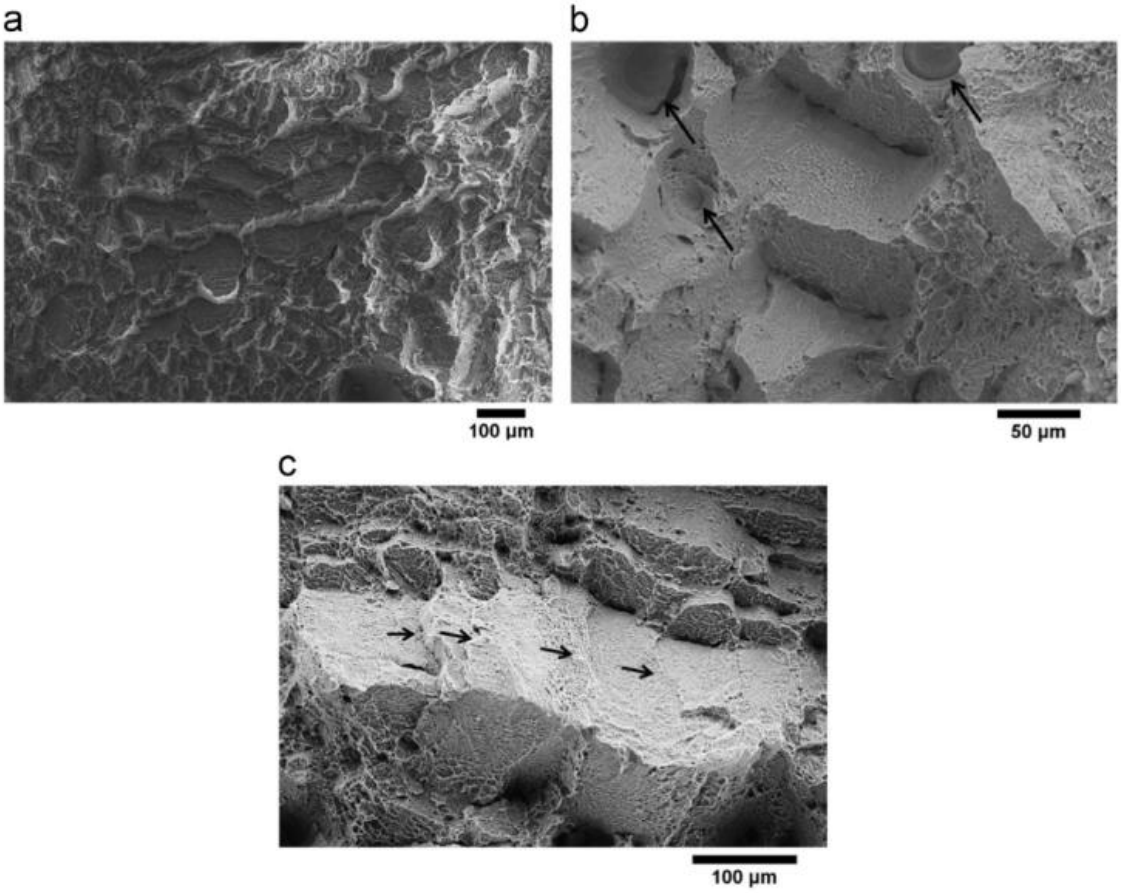

Fig 2.8 SEM images of terrace structure fractures in Ti6Al4V part produced by LPBF [49]

Cracks could be attributed to high residual stress concentration [57-59], localization of plastic deformation [60], high surface roughness [8,61], building orientation [8,62] and low ductility of material [8] according to the above studies. In addition, Engeli et al. [10] showed that micro crack phenomenon can be expected to have a correlation with the melt pool size. A number of researchers have demonstrated that pores (sharp pores in particular) could be the trigger of crack phenomenon [7,9,12,13,16,61-63]. Leuders et al. [64], Li et al. [65] and Lin et al. [60] suggested that the most populated defects (especially pores) have more negative impact on the crack initiation compared to their sizes. Edwards et al. [51] demonstrated that a large population of lack of fusion pores (more than 30 gas pores in a 1 × 1 mm^2 area) with a typical size of 80 μm would lead to crack phenomenon, as shown in Fig 2.9, which is the SEM image of the fracture surface. Their conclusion is similar to that made by Leuders et al. [64]. Günther et al. [24] demonstrated that gas bubbles with a dimension of 100 μm and lack of fusion pores about 200 μm [17] will result in crack phenomenon as well. Zhao et al. [14] declaimed similar effect can be caused by either lack of fusion pores or gas bubbles with a

size of 50 μm. Nonetheless, it was stated that lack of fusion pores with size of 50 μm would be sufficient to become a trigger of cracks without respect to their numbers [16]. Sterling et al. [12] argued that the correlation between the crack initiation and the number of pores is weak on the condition that the pores were under the size of 100 μm, unless that number of pores goes beyond a certain limit. Despite the fact that many research groups take into account the pores (lack of fusion pores or gas bubbles) are responsible for the cracks, such phenomenon can also be caused by the formation of micro cracks with a typical size of 100 μm (Fig 2.10) and the chain effect generated along with crack formation, stated by Günther et al. [24], Li et al. [65] and Leuders et al. [64].

Zhao et al. [14] suggested that the cracks usually initiate from inside pores of the samples and then propagate outwards.

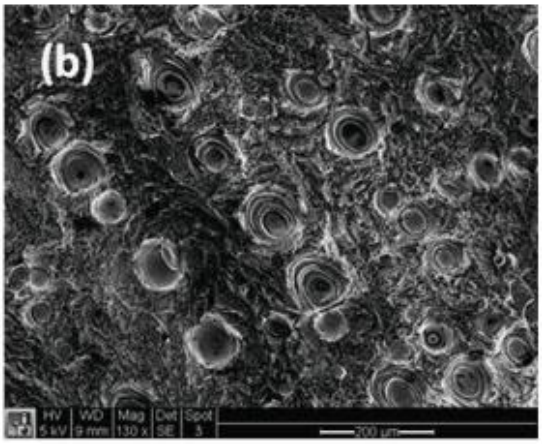

Fig 2.9 SEM image of the fracture surface with populated lack of fusion pores in Ti6Al4V part produced by LPBF [51]

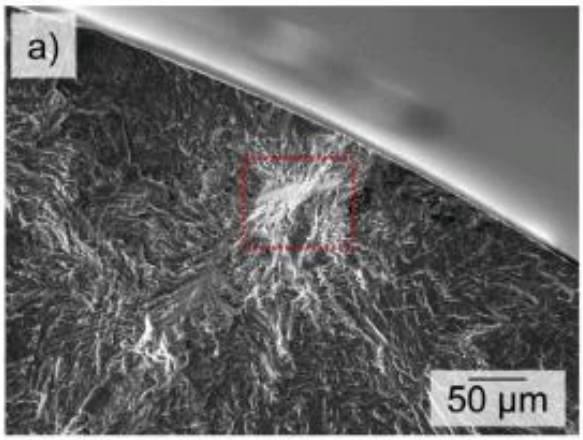

Fig 2.10 SEM image of the fracture surface with 100 μm micro crack as the nuclei in Ti6Al4V part [24] produced by LPBF

2.1.3 Balling behaviour

The weld tracks on the surface can be typically characterized with cylindrical shapes [66,67]. This sort of geometrical feature is likely to break up into rows of individual spheres in order to reduce the surface area and release the surface tension, resulting in the so-called balling behaviour in AM process [66-68]. Within the research of Li et al. [65], they classified the balling behaviour as elliptical balls and spherical balls, in which the elliptical balls are usually with dimensions of 500 μm whereas the spherical balls are typically with sizes of 10 μm. In contrast, some research groups nominated the so-called spherical balls as particles for convenience. Typical balling behaviour is shown in Fig 2.11, in which elliptical and spherical balls are stressed by the red arrows and the dotted lines.

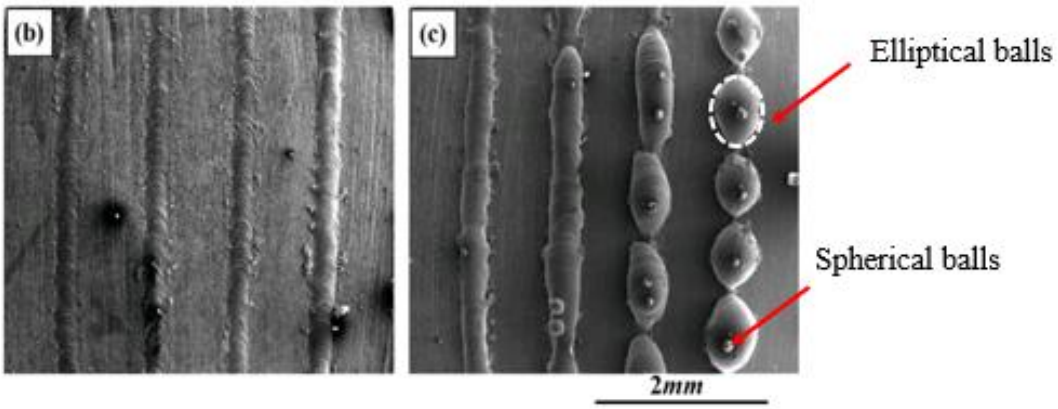

Fig 2.11 SEM images of balling behaviour in AISI 420 part produced by LPBF [16]

According to a number of related studies, balling behaviour can be attributed to many factors, which are multi-mode heat, large mass of powders [69], dynamic melting mechanism, high surface tension, low viscosity of the melted material [70], fluctuating gas flow [67,69] and uneven arrangement of local powders [71]. Lewis et al. [72] and Choi et al. [71] pointed out that non-optimum process parameters will lead to balling behaviour as well, which are high oxygen content [69,73], high scanning speed [17,28,67,69.74], low laser energy input [28,69,74] and great layer thickness [69]. Li et al. [75] discussed the cause for balling behaviour with different shapes and claimed that the elliptical balls are usually a result of insufficient energy input. However, spherical balls are typically demonstrated as the splashed un-melted particles under high scanning speed, claimed by some research groups [23,70,75].

2.1.4 Un-melted particles

Un-melted particles result when the laser beam fluctuates and the heat is not distributed properly over the melt pool. They can also be caused by irregular or oversized powders. Small un-melted particles with a size of 10's of μm were widely spread in the samples produced by Kasperovich et al. [76]. It was stated that the particles can be found at both sides of the weld tracks and in entrapped pores, particularly while the laser energy density is low [17,22].

Yadroitsev et al. [22] and Gong et al. [5] stated that laser fluctuation and reduced laser energy input could lead to the formation of un-melted particles. Khairallah et al. [9] pointed to that un-melted particles can be a result of the melting material moving up along the front wall of the depression area, spoiling onto and melting the near particles. In the case where the laser energy input is insufficient to melt all of the particles in the melt pool, new particles can contact those previous un-melted particles and form bigger spatters, pointed out by Zhou et al. [77].

Liu et al. [68] suggested that the periodical fluctuation of the intensity of spatters will interact with the laser radiation and interfere with the contact between the laser beam and the powder bed. They pointed to that the particles with a size larger than the layer thickness (specifically 50 μm ~ 100 μm) will be attached to the sides of the weld tracks, creating defects in the sample, similar to the observation acquired by Zhou et al. [78] and Kasperovich et al. [76]. These defects will not only increase the surface roughness and result in a less densified part, but will also attach badly to the adjacent layers, which is the potential trigger of crack phenomenon. Fig 2.12 [68] illustrated the histogram of distribution of un-melted particles observed in the sample, accordingly the typical size of such particles is 100 μm. Conversely, Thijs et al. [43] stated that when the spatters with a size of 25 μm coexisted with the keyhole pores with a similar size, it will potentially cause similar result. Li et al. [75] stated that the un-melted particles around 20 μm would worsen the layer bonding condition and result in the less densified samples. Darvish et al. [21] indicated that the 20 μm un-melted particles will lead to lack of fusion pores and thus result in the chain effect, yielding a severely low density of the parts.

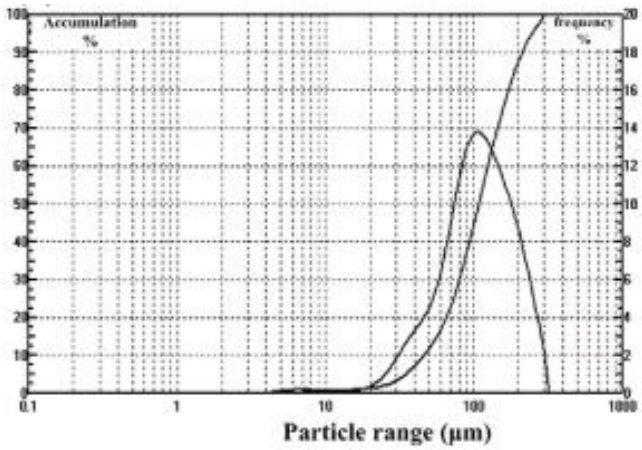

Fig 2.12 Particle size distribution in Ti6Al4V part [68] produced by LPBF

2.1.5 Pits

Pits can be characterised as the cavity structures on the surface where the un-melted particles are removed and dragged away by the recoating blade during the recoating process, as in Fig 2.13. Gong et al. [5] stated that great pits in the overlap of adjacent melt pools are not able to be removed during the remelting process despite the fact that small pits can be remelted with ease. Pits usually reduce the part density, give a rise to surface roughness and the edges of the concave structure will cause the bad connection between layers as well. Generally speaking, such pits have a similar impact to their corresponding un-melted particles, and a potentially more severe impact than the particles dragged away, in terms of their size as 1.5 times as the corresponding particles (80 ~ 150 μm).

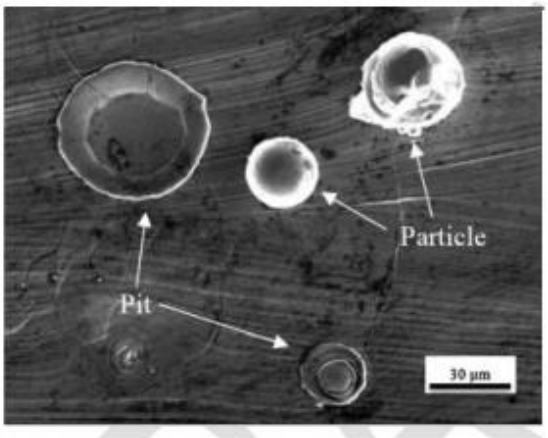

Fig 13. SEM images of pits and un-melted particles in CoCrMo part produced LPBF [19]

2.1.6 Scratches

Scratches can be characterised as the inhomogeneous tracks yielded by the process where the

particles on the surface are removed from the pits and dragged by the recoating blade along the recoating direction in the powder bed, as shown in Fig 2.14 [79]. Because the formation of such scratches is a result of the described phenomenon, the width of them is usually comparable to the diameter of the typical size of the particles, which is 100 ~ 150 μm.

Li et al. [75] suggested that on the condition that the balling behaviour is drastic, it would be a barrier of the movement of the recoating blade more severely, which yields the scratches. It is also stated that the protrusion of the melt pool as a result of the over-melting could lead to scratches during the manufacturing process [22].

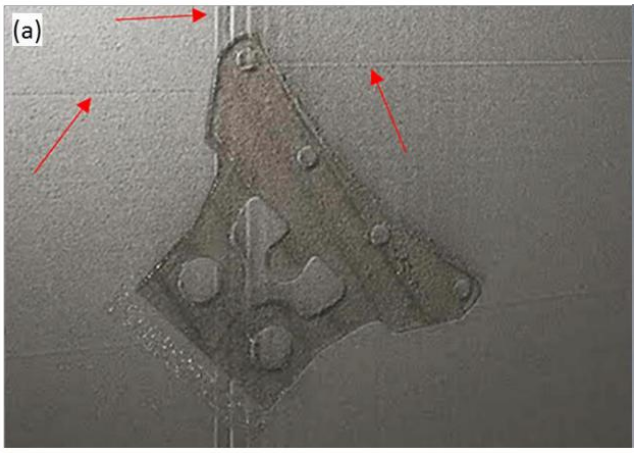

Fig 2.14 Scratches along the recoating direction [79]

2.1.7 Deformation

Deformation is generated when the heat expansion of the upper layer of the samples occurs, but the heat spread is confined by the layers underneath. When the sides of the samples, where are undertaking the greatest stress go beyond their mechanical strengths, a warpage is thus formed. Gong et al. [5] demonstrated that a large amount of heat introduced by the laser beam is not able to release quickly in the manufacturing process, resulting in deformation and causing collision with the recoating blade. An improved design of support structure can possibly reduce the deformation, however, it is not always guaranteed.

2.1.8 Signatures of defects

During the manufacturing process, not all the defects are detectable due to the limitation of measurement instrument. However , due to the correlation between signatures and the corresponding process parameters that affect them, the study of signatures should also be taken into consideration as an alternative to directly monitoring the defects, which can

dynamically adjust the process parameters to avoid further defects,

2.1.8.1 Melt pool

Melt pool is always considered the initiation site of local defects, particularly when the melt pool is less stable. An unstable melt pool can be characterised as a weld track with narrowing depth and decreasing cross-sectional width [9]. The instability of melt pool is attributed to the use of extreme process parameters (high energy input [22], low scanning speed [13] and a high gas velocity in the chamber [17]).

2.1.8.2 Weld track

It was stated that the discovered weld tracks have wavy edges and/or discontinuities [17,20]. This can be attributed to gas flow shear stress, temperature gradient and surface tension gradient [80-82].

2.1.8.3 Surface roughness

Stoffregen et al. [83] concluded that the rough surface of the LPBF parts is attributed to (1) the staircase effect caused by the accumulation of layers, (2) un-melted particles attached to the surface and sub-surface and (3) the porosity-type defects and un-melted powders, in which (1) is determined by the curvature of the surface and the layer thickness, (2) is in dependence on the powder size and (3) depends on the chosen process parameters. Surface roughness is mainly attributed to laser spot size and the layer thickness, stated by Liu et al. [84]. In addition, Gong et al. [6] found that the surface roughness will be worsened when the melt pool size is decreased.

This section attempts to give a detailed introduction to the major sorts of defects generated in the LPBF that result in the loss of densities as well as qualities of the parts, involving the appearances, locations, causes and effects of defects. A classification of defects has been done with regard to their principle properties. Also, the signature of defects has been discussed.

It is also worth noting that the LPBF is rather complicated, which involves different disturbances that can lead to defects. In addition, a defect can be a combination of different sorts of defects and one defect can be the initiator of another.

Based on the fact that all major types of the defects and the representative dimension of those which will lead to loose parts or failed parts have been discussed, a summary of the typical

sizes and shapes of the major types of defects can be conducted as Table 2.1. The typical size of the defects is divided into two sections: the defect size leading to looser parts and the defect size leading to failure, in which the latter one is more detrimental. Taking into account the objective of the project is to achieve the metrology of the defect morphology, the shape of the defects from the top view is paid more attention to. In addition, since the length/width ratio of micro cracks is low, which yields a rather small defect area, the typical metrology system does not have a good performance in distinguishing such defects from the top surface, despite the fact that micro cracks have a typical dimension of 100 μm; the deformation is also hardly detectable as it is a sort of macro defect which has much bigger dimension and spreads on the entire surface in comparison to other types of defects, and since such phenomenon would not usually cause a break on the top surface, it is rather difficult to differentiate such defect compared to measuring other types of defects which have relatively clear contours.

Table 2.1 Morphologies of major types of defects

Defects	Typical size (μm) leading to		Shapes (top view)
	Loose parts	Failed parts	
Lack of fusion	40 – 200[18]	100 – 200 [19,20]	Elongated, irregular [22]
Keyhole	-	30 [32]	Spherical [22,30]
Gas pores	100 [6,17]	100	Spherical [43]
Crack	-	100 [4,48]	Seam, curve like [48]
Balling behaviour	-	500 [66]	Spherical [67]
Un-melted particles	20 [22]	100	Spherical, elliptical (rare) [77]
Pits	80 – 150 [5]	-	Spherical, elliptical (rare) [75]
Scratches	100 – 150 [22]	-	Stripe like
Deformation	-	-	-

2.2 Review of the popular measurement / monitoring techniques for LPBF

The inspection technology for LPBF can be divided into two types: in-line inspection and off-line inspection. Among them, in-line inspection is directly implemented in the production process, it has high real-time performance and can feedback process information to the

control system in time, which facilitates decision-making in the manufacturing process and process parameter modification; offline detection has relatively high time lag, and often cannot form a closed-loop feedback system, however, offline detection usually has high accuracy and can perform comprehensive detection, which can be used as an important benchmark or supplement for in-line measuring methods.

The in-line inspection technology for LPBF can be subdivided into in-situ and extractive detection. Among them, in-situ detection can monitor the entire process of laser-substance interaction in the LPBF process, and obtain comprehensive information, which is particularly important for understanding the scientific problems and monitoring the process in LPBF, whereas extractive detection can detect the oxygen content in LPBF process. This denotes in-situ detection plays the major role in the in-line inspection.

2.2.1 In-line measurement instrument structures and information sources

2.2.1.1 Coaxial structure / visible and infrared light information in-line detection

Coaxial detection structure denotes in the implemented optical set-up, the light path and the laser beam share a common axis. Based on the coaxial detection structure, Chivel et al. [85,86] used pyrometers and photodiodes to collect optical information, to achieve in-line monitoring of the temperature distribution of the melt pool, and based on this, they studied the Rayleigh Taylor instability of the fluid. Lott et al. [87] introduced an optical system that can monitor high scanning speed and melt pool flow dynamics. It uses a coaxial optical path, a dichroic mirror, and a beam splitter to achieve the in-line inspection of the visible light and infrared light information of the melt pool area under the coaxial structure.

During the laser melting process of metal powder, a high-speed camera and a high-speed infrared camera are used to collect visible and infrared information of the melt pool in real time. Among them, the high-speed camera is responsible for real-time collection of the information of the flow in the melt pool during the melting process, and the high-speed infrared camera collects the temperature field information of the melt pool and weld tracks. Real-time data collected by high-speed cameras and infrared cameras can be then stored with a high speed and a large-capacity continuously with the use of high-speed signal processing system.

High-speed and infrared cameras are implemented at the end of the laser beam, and the images of the regions of interest of the melt pool can be captured in accordance with the deflection of the scanning galvanometer real time. The data of the temperature and flow are transmitted to the high-speed signal processing system through the high-speed optical fibre for massive data storage and real-time processing and control.

2.2.1.2 Off-axial structure / visible and infrared light information in-line detection

In comparison with the coaxial structure, the off-axial optical structure has many advantages including a simple optical path and mechanical structure. It can be used for in-line inspection and research without the need to modify the existing AM machine. Therefore, related research was carried out by many research institutions using this optical set-up currently [88]. Nevertheless, this leads to the increase of workload in the research of subsequent image pre-processing and defect detection algorithm research compared to the information obtained by the coaxial structure.

Grasso et al. [89] pointed out the phenomenon that the accumulation of defects in the previous layers in the LPBF process will fail the building of the subsequent layers, and the traditional micro computed tomography (micro-CT) and ultrasonic non-destructive testing can only be processed offline so that the errors process cannot be corrected in real time. To tackle such problem, an off-axial structure was implemented to be able to monitor the manufacturing process and the generated defects with specific in-depth statistical methods.

Krauss et al. [90] conducted an evaluation of the stability of the LPBF process and the quality of parts by collecting the layered temperature distribution data during the LPBF process. The layerwise monitoring and evaluation of the melting and solidification process was achieved in the way of implementing a micro-bolometer off-axially. This helped to identify the hot spots in the early stages of laser melting process, thereby effectively avoiding faults and improving the stability of the manufacturing process. In addition, Krauss et al. pointed out that it is possible to construct potential indicators to predict the quality of parts by introducing spatial analysis methods and to use the combination of data modeling and thermal imaging tests to

study the relevance between the thermal diffusivity and the porosity. The results show that thermal imaging technology is a feasible manner to monitor the manufacturing process.

In most of the literature about the in-line monitoring technology for LPBF process, the images of melt pool, weld tracks and layerwise images were used as the information sources to detect possible defects. Aiming to improve the stability of LPBF process, Repossini et al. [91] collected the layerwise images with the use of an off-axial structure, obtained the statistical descriptor in relation to spattering behaviour through image segmentation and feature extraction methods and acquired the corresponding relationship between the spattering descriptor and the different laser energy levels using the logistic regression model. In a similar vein, Yang et al. [68] conducted cutting-edge research on spatter formation in LPBF process.

2.2.1.3 Photodiode in-line detection

Photodiode is a photoelectric sensing device that can convert optical signals into electrical signals. It can output corresponding analog electrical signals according to the illuminance of the received light or switch between different states in digital circuits. Such technique has been widely used in modern industry. In LPBF process, the process that high-energy laser melts the powders will cause a strong radiation. Therefore, it is feasible to use a photodiode to monitor the melt pool behaviour.

In order to optimise the process of producing ceramic parts, Kai et al. [92] used arrays of photodiodes to improve the accuracy of the collected melt pool information during LPBF process for the purpose of optimising the melt pool behaviour. Based on this system, the influence of laser power on the behaviour of melt pool and the corresponding relationship between the melt pool data and the defect classes were also analysed.

2.2.2 Offline detection technologies

2.2.2.1 Micro-CT technology

Micro-CT technology was invented in the 1980s, and the first commercial micro-CT system appeared in 1999. It has a micron-level resolution and can non-destructively detect the micro scale inside an object. In the welding industry, advanced micro-CT technology is used to

conduct a more detailed analysis of welding defects, and it was found that welding defects normally have more complex three-dimensional structures. This implied that the defect morphology information given by two-dimensional analysis methods (optical microscope, scanning electron microscope, X-ray inspection, ultrasonic) is often insufficient, so it is difficult to accurately analyse its formation mechanism, yielding the ineffectiveness of non-destructive testing.

AM parts have internal defects similar to welded castings. Therefore, the application of micro-CT technology can be transferred to the quality inspection and characterization of the internal defects and structure of AM parts.

S. Van Bael et al. [93] intended to build Ti6Al4V parts with a controlled complex porous structure with LPBF, but the as-built parts appeared to be quite different from the corresponding CAD model. In order to optimise the robustness and controllability of the forming process of the porous Ti6Al4V structure, the off-line micro-CT technology was applied to compensate the process parameters and reduce the dissimilarity between the CAD model and the AM parts in terms of their size, shape and mechanical properties. Xin et al. also carried out research on the application of micro-CT in the characterisation of AM parts [78]. In addition, Bobel et al. [94] also achieved the inspection of the internal structure of AM parts with the use of the in-situ synchrotron X-ray computed tomography (XCT) imaging technology, and the inspection results had been verified by SEM and EBSD.

2.2.2.2 Optical metrology instruments

Optical measuring instruments have been increasingly used in PBF. For instance, in [95], a confocal microscope was used to capture areal topography, and in [96-98], coherent scanning interferometry was used. More specifically, for FV, previous work has shown that this technology provides a good compromise between the quality of measuring results, versatility, ease of operation and measurement time [3,99]. These advantages have suggested the use of FV for the measurement of AM surfaces [99-105].

Thompson et al. In [106] compared various measurement techniques on the top surface of AM parts. In their work, FV, coherent scanning interferometry (CSI), confocal microscopy

and XCT were used to measure and compare the same surface. Furthermore, their work focused on the impact of various surface features on the measurement, and more importantly, the impact of each measurement technique on the ability to capture the same surface.

Gomez et al. In [97] studied the influence that the measurement configurations of CSI had on the measurement of different kinds of AM surfaces, this work provided a method that can optimise the optical measurement system for AM surfaces and understand the interaction between the instrument and the surface. Further research is needed to determine the optimised configuration of other measurement technologies and the impact that modifiable measurement parameters have on the final measuring results.

3. Methodology

The research methodology is designed as follows: samples with different materials and sizes are chosen to be measured with surface topography measurement instruments to determine their optimal settings. Then an optimum filtration method is chosen to characterise the measured surface. Finally, the defect detection is achieved using multiple ML techniques.

More specifically, to investigate the manner in which the particles are distributed on the surface of AM parts and comprehend the potential particle distribution difference in samples of various structures and materials, Aluminum super-alloy regular blocks, Ti6Al4V regular blocks blockand Inconel 718 regular blocks have been selected for the measurement.

FV or FV microscopy (FVM) is a high precision optical measuring technique that has been applied in a great variety of areas, particularly in surface roughness metrology. It is defined as "surface topography measurement method whereby the sharpness of the surface image from an optical microscope is used to determine the height at each position across the surface" [99].

FV is able to collect a set of images with similar focuses in the way of moving the instrument and object in relation to each other, then the focus for each plane is to be calculated. Following this process, the corresponding depth of field will be determined according to the focus for the planes with the use of a fitting algorithm. The technique is typically used for optical surface metrology to measure the form, surface roughness of samples. However, there is a huge limitation of using FV to do form detection while the surface roughness of the samples is too low, which means there are not many steep or complex structures on the surface as the system is specifically designed for measuring the height difference between adjacent or close planes on the surface. In addition, it is not capable of measuring the samples with translucent surfaces as well. The working principle of the technique is shown in Fig 3.1 [100].

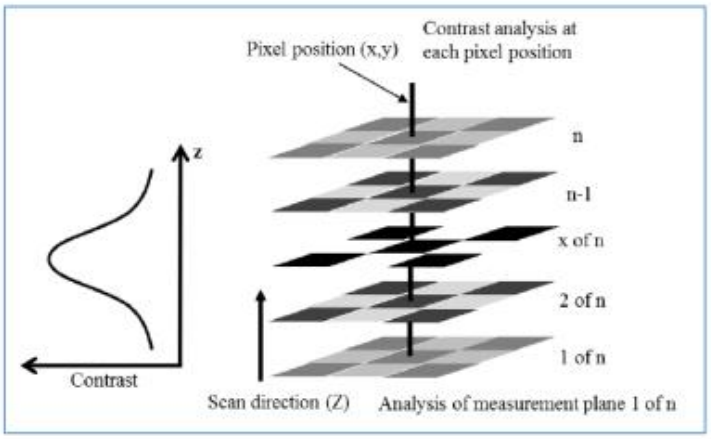

Fig 3.1 Working principle of FV [100]

Although the FV system can provide surface feature characterisation, it is not an ideal choice for in-line measurement due to the limited working distance. Among the measurement instruments for measuring the surface topography of AM parts, FP is a method that can measure features that are hundreds of microns in size across the entire powder bed. In order to achieve similar resolving power compared with the FV system, a FP system has been built.

Following the measurements of the AM parts on both FV and FP systems, specific filtration method needs to be selected to optimally characterise the representative features (i.e. defects) on the measured surface. In this thesis, several typical filtering techniques that can extract roughness components including particle features without removing the form, which are classic Gaussian regression filter, robust Gaussian regression filter 'opening + closing' morphological filter and 'closing + opening' morphological filter, are compared. Subsequently, the optimal filtration method to extract the defect features is determined.

With the use of selected filtering method, the processed measured surface can be used by ML, to achieve the objective of detecting defects. This thesis aims to achieve the defect detection in the manners of classification (classifying different partitions of the surface into defective area and non-defective area) and regression (segmenting defects with the use of neural network (NN)). Both unsupervised ML and supervised ML methods are assessed to test the suitability and defect detecting ability.

Regarding ML, two ML types, including supervised ML and unsupervised ML, and three

different ML methods have been used to achieve defect detection in different manners. As a typical ML method, principal component analysis is capable of categorising the input instances with similar features into the same classification so as to define the captured images as ‘defect’ images or ‘no-defect’ images. In the following section, two supervised ML methods are of use to further enhance the applicability of ML in defect detection: with the establishment of convolutional neural network, defects can be classified in a more accurate and efficient manner after the training process. In addition, another NN called U-Net was established. Its major advantage is it is not limited to classifying the images into distinct types, but is also able to segment the defect, so that the full information of defects, including size and geometry, can be acquired.

4. ML applications for defect detection / feature extraction in LPBF

4.1 ML for defect detection and prediction

Two major manners of defect detection have been widely applied in the investigation into additively manufactured samples, one is mainly based on the classic digital image processing technique to characterise the edges or the contours of the detrimental features and thus achieve the feature recognition, while the other is resting on the newly evolved and vastly developed machine learning method. There are several advantages and disadvantages of such methods, which are:

Digital image processing

1) Robust algorithm to threshold certain relatively simpler features or objects;

2) Requires less amount of computation and memory;

3) Algorithms may not be suitable for additively manufactured surface since there are widely spread irregular patterns all over the surface in terms of the process signatures or the defect features to be extracted;

4) Albeit digital image processing has been given a credit to in the field of post-processing analysis of AM, it is difficult to apply such technique in real time;

ML

1) Able to identify the features with complex geometries without advanced thresholding techniques for the most part;

2) Effective for defect detection when the training dataset is well established, so that a new defect in the test dataset can be identified in nearly real time as long as it shares a similar feature with any defects in the training set;

3) Requires very high-specification CPU and huge memory for computation;

4) A very informative training dataset including different geometries of the features to be compared against is always desired in order to secure a high feature recognition rate;

To efficiently give the AM machine an instant feedback on how well the manufacturing condition is, being able to detect the defects in real time or immediately after the fabrication process is desired. As such, in recent times, ML is preferred for providing a relatively fast result with more intuitive algorithm, despite the fact that it requires a high-end digital

processor. The following sections reviewed the ML application in defect detection for various data.

To facilitate the understanding of some concepts discussed in the following chapters, a detailed description of those concepts are given as follows.

1) Bayesian inference

Bayesian inference is a method of inference statistics. This method uses Bayes' theorem to update the probability of a particular hypothesis when there is more evidence and information. It is one of the most important techniques in statistics (especially in mathematical statistics).

2) Naive Bayesian classifier

In ML, the naive Bayes classifier is a series of simple probability classifiers based on the use of Bayes' theorem under the assumption of strong (naive) independence between features. The classifier model assigns class labels represented by feature values to the problem instances, and the class labels are taken from a limited set. A series of algorithms based on the same principle are used to train this classifier and all naive Bayes classifiers assume that each feature of the sample is not related to other features.

3) Bag of keypoints

Bag of keypoints is an image feature extraction method. It draws on the idea of text classification (Bag of Words), abstracts many representative ‘keywords’ from images, forms a dictionary, and then counts the occurrences in each image. The number of ‘keywords’ is used to obtain the feature vector of the picture.

4) Convolutional neural network (CNN)

CNN is a type of feedforward neural network that includes convolution calculation and has a deep structure. It is one of the representative algorithms of deep learning. It imitates the construction of biological visual perception mechanism. The convolution kernel parameter sharing in the hidden layer and the sparsity of the inter-layer connections enable the CNN to learn the features in the inputs with a small amount of calculation.

5) Principal component analysis (PCA)

In multivariate statistical analysis, PCA is a method of statistical analysis and simplification of datasets. It uses orthogonal transformation to linearly transform the observations of a series of possible related variables, and then project the values of a series of linear unrelated variables, which are called principal components (PCs). PCA is often used to reduce the dimensionality of a dataset, while retaining the features in the dataset that contribute the most to variance. This is done by keeping the low-dimensional PCs and ignoring the high-dimensional PCs

6) Support vector machine (SVM)

SVMs are supervised learning models and related learning algorithms that analyse data in classification and regression analysis. Given a set of training instances, each training instance is marked as belonging to one of the two categories, the SVM training algorithm creates a model that assigns the new instance to one of the two categories, making it a non-probabilistic binary linear classifier.

7) Support vector data description (SVDD)

The basic idea of SVDD is to take the object to be described as a whole and build a closed and compact hypersphere, so that all or as much of the object described is enclosed in this sphere, whereas no or as less of the object falls in. It is a single-value classification algorithm that can distinguish between target samples and non-target samples, and is usually used in fields such as anomaly and fault detection.

8) Non-parametric Bayesian Dirichlet process mixture model

The Dirichlet process mixed model is a non-parametric Bayesian model. It can be considered a classification method, it can infer the number of classifications from the data, without the need to specify the number of categories.

9) Probabilistic neural network (PNN)

PNN is a feedforward neural network developed from a radial basis function network. Its theoretical basis is the Bayesian minimum risk criterion (Bayesian decision theory) and it is suitable for pattern classification.

10) Sparse representation

The purpose of sparse representation is to use very few features to represent the signal in a given super-complete dictionary, so that a more concise representation of the signal can be obtained more easily, and the signal can be further processed with ease.

11) Decision tree

Decision tree is composed of a decision diagram and possible outcomes (including resource costs and risks) to create a plan to reach the goal. It has a special tree structure and is used to assist decision making. It acts as a decision support tool that uses a tree-like graph or decision model, including random event results, resource costs and practicality.

12) Blob

A blob is an area where some properties of the image are constant or nearly constant where all points in the blob can be considered similar to each other.

13) Binary local patterns

Binary local patterns is a non-parametric local texture feature descriptor with simple theory and high computational efficiency. Due to its high feature discrimination capability and low computational complexity, it has been widely used in the fields of image analysis, computer vision and pattern recognition,

14) Local edge descriptors

Local edge descriptors is a simple and effective shape representation method, which has been widely used in target detection and target recognition. The extraction process is divided into main steps including image segmentation and calculation of the edge histogram of sub-sectional images.

15) Co-variance matrix

In statistics and probability theory, each element of the co-variance matrix is the co-variance between each vector element, which is a natural extension from a scalar random variable to a high-dimensional random vector.

16) Eigenvalues and eigenvectors

If the co-variance matrix A has n dimensions, and λ and the n-dimensional non-zero column vector x satisfy $Ax = \lambda x$, then λ is called the eigenvalue of A, and x is called the eigenvector of A corresponding to the eigenvalue λ.

17) Depthwise convolution and pointwise convolution

Depthwise convolution projects a convolution on each input channel. Therefore, the number of output channels is the same as the number of input channels. Pointwise convolution is a convolution with a 1×1 kernel size, which combines the features created by depthwise convolution

18) Batchnorm

Batchnorm can resolve the problem of gradient disappearance in ML by changing the activation direction into a unit normal distribution, which speeds up the training process.

19) Rectified linear unit (ReLU)

ReLU, also known as the modified linear unit, is an activation function commonly used in artificial NNs (ANNs), usually referring to the non-linear function represented by the ramp function and its variants.

20) Neuron activation function

Each neuron node in the NN receives the output value of the previous layer of neuron as the input value of this neuron, and passes the input value and the input attribute to the next layer (hidden layer or output layer). In a multilayer NN, there is a functional relationship between the output of the upper node and the input of the lower node. This function is called the activation function.

21) Weight matrix

Weight matrix contains the parameters within a NN that transforms input data within the network's hidden layers. As inputs enter the nodes, they get multiplied by a weight matrix and the resulting output is either observed, or passed to the next layer in the neural network. Often

the weights of a neural network are contained within the hidden layers of the network.

22) Cluster

Clustering is a typical unsupervised learning method, which reveals the intrinsic properties of the data through the learning of unlabeled training samples and provides a basis for further data analysis.

23) Categorical cross-entropy cost function

The cross entropy cost function is a way to measure the predicted value and actual value of an ANN. In comparison with the quadratic cost function, it can promote the training process of ANN more effectively.

24) Backpropagation

Backpropagation is the abbreviation for "error backpropagation", which is a common method used in combination with optimisation methods (such as gradient descent) to train ANNs. This method calculates the gradient of the loss function for all weights in the network. The gradient will be fed back to the optimisation method to update the weights to minimise the loss function.

25) Overfitting

Overfitting is a modeling error that occurs when a function fits a limited set of data points too closely. Overfitting models usually take the form of overly complex models to explain the characteristics of the data being studied.

26) L2 regularisation

L2 regularisation refers to the sum of squares of each element in the weight matrix. In order to optimise the regularisation term, the sum of the parameter squares will be reduced. Therefore, L2 regularisation will choose weight parameters with small values, which is mainly used to prevent the model overfitting.

27) Dropout

Dropout refers to that during the training process of the deep learning network, the NN unit is temporarily dropped from the network according to a certain probability. Among the regularisation methods, dropout is a useful and successful technique that can effectively tackle overfitting.

4.1.1 Defect detection with visual data

Aminzadeh and Kurfess [107] developed an in-line monitoring system to examine the porosity and part quality in LPBF with the use of computer vision and Bayesian inference. They created a labeled dataset of features with defects and without defects, from the layerwise images. They extracted frequency-domain features from those images and used a Bayesian classifier to identify defective parts and non-defective parts.

Scime and Beuth [108] used computer vision and ML technology to detect and classify defects in the powder before fusion as opposed to using the layerwise images captured after laser interaction. They studied six different types of defects on the powder bed captured in the labeled images. The bag-of-keypoints ML technology for detecting and classifying defects can detect the existence of defects in 89% of the cases, and the accuracy of correctly identifying the types of defects can reach 95%. In addition, the authors demonstrated that the accuracy can be further improved by implementing a multi-scale CNN for the purpose of autonomous defect detection and classification [109].

Zhang et al. [110] used principal component analysis (PCA) with SVM and further applied CNN to identify features in the manufacturing process, in which the features are melt pool, spatters. The recognition accuracy can reach 92.7%.

However, all of the above described ML applications were exclusively able to detect relatively large scale defects or process signatures including melt pool. Furthermore, since the grey scale images were captured with the use of computer vision techniques, the results were not guaranteed to be representative of the real surface topography.

4.1.2 Defect detection with multi-sensor data

As previously described, the data collected from in-line monitoring system has mixed types. The data registration and fusion from multiple sensors provides adequate conditions for defect detection. Hence, more and more research was conducted on involving multi-sensor data

fusion for in-line monitoring.

Grasso et al. [111] explored data fusion methods to combine in-situ data from multiple sensors installed in an electron beam PBF system. Support vector data description (SVDD) ML technology was used to automatically detect defects given the multi-sensor data. The limitation of this method is that it is only suitable for mass production of the products with the same pattern.

Rao et al. [112] incorporates data from heterogeneous sensor suites embedded in the in-line monitoring system, in which the suite includes infrared temperature sensor, real-time miniature video borescope, thermocouple and accelerometer. Non-parametric Bayesian Dirichlet process mixture model and evidence theory were used together to detect defects from the data collected from the fused sensor, a prediction accuracy of up to 85% were achieved. This performance was greater than some other existing methods (Probabilistic Neural Networks, Naive Bayes Clustering and SVM).

Petrich et al. [113] and Gobert et al. [114] used multi-sensor data fusion to detect discontinuity defects (pores and un-melted particles) in LPBF. They combined matching sensor data (8 sets of layerwise images of the powder bed before and after sintering under varying lighting conditions) and heterogeneous sensor data (XCT scanned results). Ground-truth labels (abnormal or normal) extracted from CT scans were used to train NN, SVM [113], and SVM ensemble classifiers [114] to detect defects directly from images. In comparison to only using images under a single lighting condition for classification (with an accuracy of 65%), the ensemble classifier can reach a higher classification accuracy (85%) under different lighting conditions.

Although more areal surface topography can be acquired using multi-sensor data, there are still limitations to detecting defects against data collected from different sensors. For 1) there is difficulty in the data registration and data fusion as the data has multiple sources and types; 2) since the multi-sensor suite normally consists of advanced sensors, including infrared temperature sensor, real-time miniature video borescope, the entire setup is usually expensive and not cost-effective; 3) some measurement suites were installed outside the protective glass of the manufacturing chamber, as a result, the measurement accuracy and the image resolution was weakened.

4.2 Part inspection and validation

ML techniques are also used for AM part inspection. They are primarily implemented for surface metrology, defect detection and classification, using offline measurement results, e.g. XCT data.

Tootooni et al. [115] classified the dimensional change in parts made by FDM based on the spectral graph theory. They used Laplacian eigenvalues as the extracted features from laser scanning 3D point cloud data, and classified the dimensional change with the combination of different supervised ML techniques, including sparse representation, k-NN, NN, naive Bayes, SVM and decision tree. Among them, sparse representation technology provided the highest classification accuracy.

Liu at al. [116] proposed an enhanced layerwise spatiotemporal log Gaussian Cox process (ALS-LGCP) model to determine the spatial distribution of pores in the layers of AM parts and trace the continuous evolution in between layers. They applied the ALS-LGCP to binder-jetted parts, and used Bayesian predictive analysis to predict the areas that are prone to voids and made the prediction accuracy rate reach 85%.

Senin and Leach [117] used multi-sensor data fusion and ML to develop an intelligent, information-rich surface metrology system. They pointed out that because AM parts usually have complex shapes and different material properties, more advanced measurement methods are required.

However, the disadvantages of offline part inspection and validation are obvious as it can only be done when the manufacturing process is finished and the part is moved to a new measurement environment. Especially for XCT inspection, the inner structure given by the 3D reconstructed results can be barely used as reference to the areal surface topography of AM parts.

In order to tackle the above limitations in the ML application for defect detection, this thesis aims to 1) be able to inspect the defects with micro scales which can cause less densified and failed parts; 2) limit data types and number of sensors to reduce the potential error incurred by data fusion and reduce cost; 3) integrate the setup close to the surface of AM parts to acquire a better resolution; 4) measure AM parts at its original as-built position to achieve in-line inspection.

5. Measurements of AM surfaces

5.1 Samples

3 samples were produced by LPBF for this work, which are an Aluminum super-alloy regular block, a Ti6Al4V regular block and a maraging steel regular block. The detailed specification is listed in Table 5.1. Among them sample 1 and sample 3 were measured by FV whereas sample 2 was measured by FP. Sample 2 was specifically designed and made to be measured by FP as it is suitable for measuring larger surface due to its larger field of view and longer depth of field, in comparison to FV.

Table 5.1 Materials, commercial systems and specifications of the samples

Sample	Material	Commercial system	Specification
1	Ti6Al4V	Renishaw 250	10 mm × 10 mm × 10 mm
2	Ti6Al4V	Renishaw 250	100 mm × 100 mm × 5 mm
3	Maraging steel	Renishaw 250	20 mm × 20 mm × 20 mm

5.2 FV measurement setting optimisation

In order to provide accurate, reliable, and effective measurement results, it is important to use appropriate instrument parameters when performing measurements on the Alicona IF G5 FVM. However, this choice depends on the specific application and instrument users. However, for surface measurement of additively manufactured parts, some general rules can still be followed.

5.2.1 Utilise the correct objective lens

In FVM, up to 4 different sets of objective lenses that can be chosen from, which are 5×, 10×, 20×, 50×. In order to select the appropriate objective lens, strict judgments are required, as this will affect the field of view, the illumination source and the choice of lateral and vertical resolution. In general, the higher the magnification of the selected objective lens, the more accurate the measurement result. For this reason, a 50× objective lens is preferred.

5.2.2 Select the right illumination source

On top of choosing the objective lens, it is also necessary to choose the correct light source to effectively illuminate the measured area. Since the geometry of the weld track on the surface of AM parts is not very smooth, it is advantageous to apply the ring light to increase the aperture of the optical system.

5.2.3 Choose the optimal instrument resolution

The vertical resolution is used by the FV instrument to indicate the distance between the images in the in-focus picture stack, whereas the lateral resolution is a term used by the FV to determine the size of an area in which the contrast of each point in each image in the stack is determined.

In the experiment, the lateral and vertical resolution values should be selected considering the range automatically suggested by the instrument software. To be more specific, for the lateral resolution, on the basis of the selected magnification and illumination source, the recommended value was chosen as 1 μm, due to a) it was within the acceptable value range recommended by the instrument software; b) it provided a small enough distance between the images in the stack. For the vertical resolution, the default recommended value of the instrument software was chosen as 50 nm, which was the center value within the acceptable value range recommended by the instrument software.

5.3 Fringe projection measurement

The FP imaging technology is realised by replacing a camera in stereo vision with a projector. The light source projects a coded image according to the rules and patterns defined by the user to the measured object to conduct an active morphological measurement. The coding pattern is deformed by the modulation of the surface topography of the object, and the deformed structured light is captured by a camera at another location. The 3D shape of the object can be determined by the positional relationship between the camera's projection light source and the degree of structured light deformation. .This technique is able to measure the features with typical size of hundreds of microns, for such reason it can be used for the metrology of AM parts. In this work, The FP consists of 4 machine vision cameras and an Optoma UHD550X projector with a resolution of 1920 × 1080 pixels. The sample to be

measured is a metal Ti6Al4V additively manufactured part with a size of 50 mm × 50 mm. The principle of the measurement is that two types of fringes, which are sinusoidal and binary fringes, will be projected onto the sample and the corresponding images will be captured by the 4 machine vision cameras from different perspectives, where the sinusoidal fringes are used for the computation of the phase map, whilst the phase map unwrapping process is achieved with the use of the binary fringes. After establishing four sets of point clouds collected from different angles, the datasets need to be aligned to ensure an integrated polygonal mesh with good coverage. The alignment operation has been conducted in PolyWorks with the combination of the use of manual pre-alignment and best fit object to reference functions. Following such operation the height map of the polygonal model could be computed in accordance with the standard deviation to the reference plane. The measured and aligned polygonal mesh is shown in Fig 5.1.

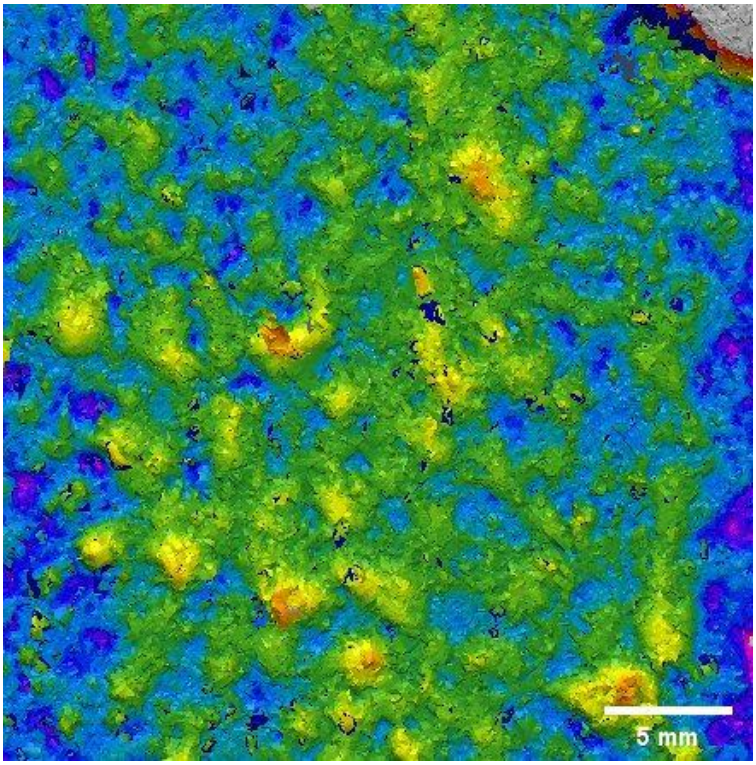

Fig 5.1 Measuring result of sample 2 with FP system

As formerly mentioned, spatters and particles are the results of the interaction with the laser. They can either potentially obstruct the recoating process of recoating blade or result in fewer bonds in between layers and thus cause less densified parts, and even a chain effect and crack initiation. Considering the importance of such phenomena, the research mainly focused on the

establishment of ground-truth data for these phenomena and subsequent in-line measurements.

6. Machine learning database preparation

In order for the measurement results to be effectively used by machine learning, they need to undergo some specific pre-processing. The filtration method able to help understand the correlation between the surface topography of AM parts and AM processes should be selected. Then for the purpose of expanding the number of images for machine learning to obtain better accuracy, data augmentation operation is carried out.

6.1 Filtering methodologies selection and comparison

For AM surfaces, the un-melted particles and pores are considered "outliers" because they have obvious high or low values in comparison to the surrounding data. Robust Gaussian filters provides robustness against such outliers by including robust statistical estimators into the filtering process. Additionally, since polynomial fitting is incorporated into the filter, there is no need to remove the surface form. An alternative to such method is the morphological filter. It is based on two morphological operations, dilation and erosion, which work with the use of structuring elements (circular disks / spherical balls). For example, in order to dilate the profile below by a disk of a certain radius, the disk rolls over the surface and the path of its centre is recorded (red line). Dilation can enhance peaks and fill holes. In contrast, if the disk is rolled below the surface, it is called an erosion.

As the previously described filters in Gaussian series, morphological filter is not required removing the form as well. The two most commonly used morphological filters are called the closing filter and the opening filter, which are detecting the upper and lower envelopes of spherical balls. More specifically, when erosion is followed by dilation (the disk rolls over the profile and then over the created erosion line), it is called an opening filter that creates the lower envelope. The envelope opens holes and pores while following the lower shapes of peaks and hills. Whereas when the process is reversed (dilation is followed by erosion), it is called a closing filter which creates the upper envelope. By applying different sizes of the spherical balls, different corresponding scales of features can be identified in a sense that surface form can be measured by the application of large disks / balls, waviness components can be measured by the medium disks / balls and the small disks / balls are able to identify small features including particles and spatters. As a rule, the opening filter is able to

characterise the weld tracks and filter out particle structures in that the opening filter is the lower boundary of profile, the peaks on such profile can be successfully extracted. In contrast, the closing filter is used when valley or pore structured is wanted to be extracted. Concretely, suppose the purpose of such morphological filtration is to extract particle features, then the combination of 'opening + closing' filtering operation is preferred to enhance the peaks on the profile with the opening filter meanwhile suppressing the valley features with the closing filter. On the contrary, 'closing + opening' filter can be applied provided the pore structures or features are dominant on the surface texture.

In order to identify which filtration method is more suitable for the feature extraction of additively manufactured surfaces, the comparison between the Gaussian regression filter, robust Gaussian regression filter, 'opening + closing' filter and 'closing + opening' filter have been tested respectively. For the purpose of observing the difference among them, the comparison of the four different types of filters were carried out on a selected profile data on the measured surface of the aforementioned Ti6Al4V regular block. For the Gaussian regression filter and the robust Gaussian filter, the cut-off (λ_f) was chosen as 0.12 mm whereas the radius of the spherical balls was set to 0.1 mm to extract the waviness component including the wavy shape of weld tracks and suppress the influence of un-melted particles, for the latter two morphological filter. It can be viewed from the profiles illustrated in Fig 6.1 through 6.4, the robust Gaussian regression filter as well as the 'opening + closing' morphological filter demonstrated comparatively the superior results since the peaks representing the particle and spatter features were extracted, meanwhile within the profiles where the classic Gaussian regression filter and 'closing + opening' filter were applied, the waviness was not entirely removed in the extraction results and the profile at the boundaries of the particle feature differs from the norm significantly. Because of such reason, the robust Gaussian regression filter and the 'opening + closing' filter were selected as the candidates as regards filtration.

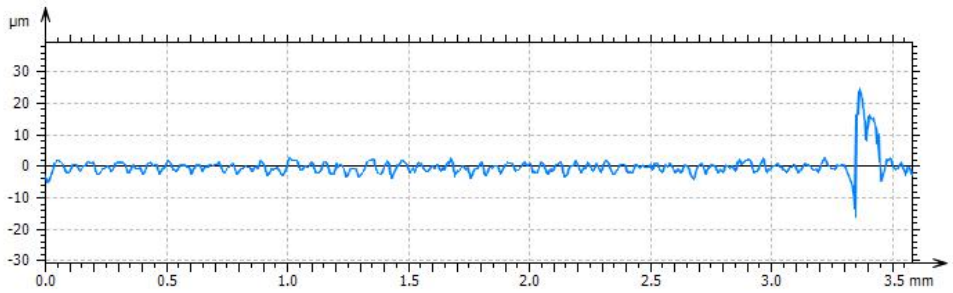

Fig 6.1 The utilisation of Gaussian regression filter

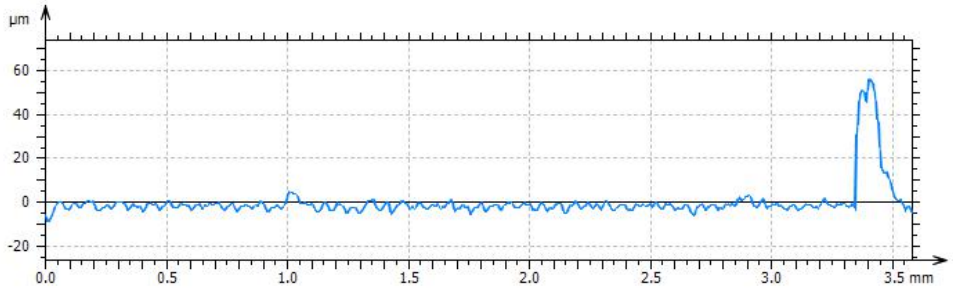

Fig 6.2 The utilisation of robust Gaussian regression filter

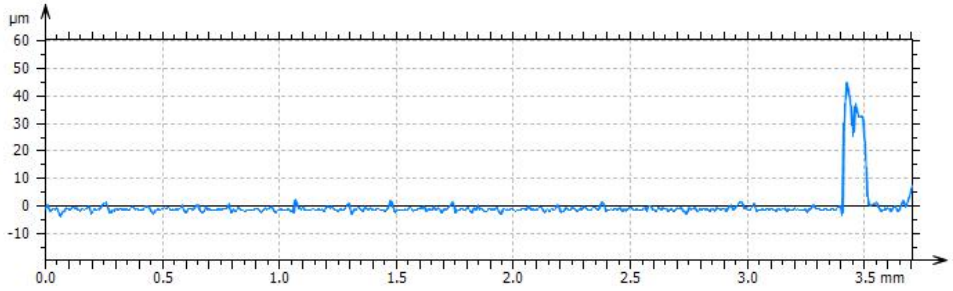

Fig 6.3 The utilisation of 'opening + closing' filter

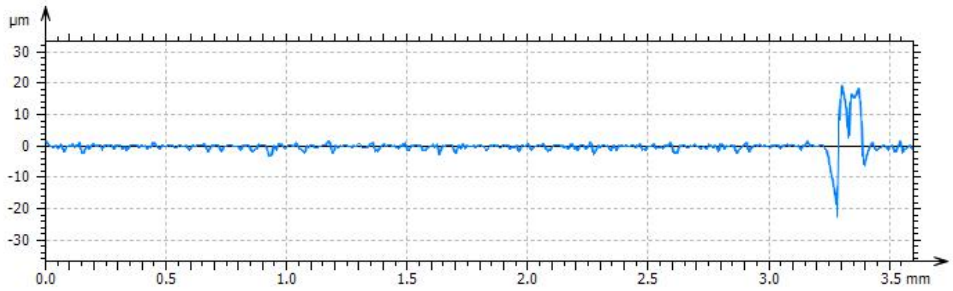

Fig 6.4 The utilisation of 'closing + opening' filter

6.2 Data augmentation

As commonly acknowledged, rich and high-quality data is the key to training a good ML model. However, collecting data manually is a time-consuming and laborious task. More importantly, it is difficult to obtain adequate data in specific fields when the sample size is small or the experiment is hard to repeat. As in this thesis, the number of samples is limited,

and the 10 mm × 10 mm measurement area of the instrument (field of view) further limits the size of the dataset.

The use of some specific procedures to expand the dataset has become an effective way to solve the lack of data, which can increase the size of the training set by 10 times or more. The model trained in this manner is usually more robust and reduces overfitting.

Data augmentation refers to appropriate transformation of the original data to achieve the effect of expanding the data set based on some prior knowledge, while maintaining specific information. Specifically for image classification tasks, the following transformations can be performed on each image in the training set while keeping the image category unchanged: random rotation, translation, scaling, cropping, filling, flipping left and right, where these transformations correspond to the observation results of the same target at different angles; addition of noise disturbances to the pixels in the image, including salt and pepper noise, Gaussian white noise, color conversion, change of brightness, clarity, contrast, sharpness. In practice, multiple data augmentation operations are often used concurrently.

7. Defect detection with the application of different types of machine learning algorithms

ML has been extensively studied in the past decades. It is a field of study where the computers can learn from the input data with little explicit manual programming incorporated to solve classification and prediction problems.

The ML methods can be classified into two major types: supervised ML and unsupervised ML. For supervised ML, the input data is split into two datasets: the training set which contains not only the instances, but also the expected output of each input instance according to their relationship (labels), and the test set used to test and evaluate the applied ML algorithm. The relationship between the instances and their corresponding labels can be learnt by the ML algorithm and a model describing such relationship is generated. Subsequently, the test set is fed to such model to provide the predicted results. Such sort of ML method is able to resolve classification or prediction problems. In contrast, unsupervised ML the dataset does not need to be labelled. Depending on the model being chosen, unsupervised ML is able to categorise the input instances with similar features into the same cluster or classification. Less manual work is involved in unsupervised machine learning however the classification result may not be as obvious as well-trained supervised machine learning models. Some reasons why machine learning has been extensively researched in recent years are:

1) Addressing the issues existing in traditional approach (e.g. digital image processing) time-consuming, energy wasting;

2) Tackling complicated problems which cannot be resolved in a traditional approach;

3) Coping with fluctuating environments by consistently learning upon new input data and refining the model;

4) Being able to get insights from big and complex data;

There are mainly two ways of achieving defect detection, either classifying the defects on the surface of AM parts into different types, or segmenting the defects to provide the detailed geometries of the defects. As aforementioned, both supervised ML and unsupervised ML methods are capable of resolving the defect classification problems, whereas defect segmentation can exclusively achieved using supervised ML. In this thesis, principal component analysis (PCA) as an unsupervised ML method and MobileNet as a supervised

ML method were used to fulfil*l* the defect classification as they are *both* powerful in coping with complex and high-dimensional data with many features for the purpose of defect categorisation. Additionally, in order to understand the full information of defects, including size and geometry, the defects need to be segmented during the defect inspection. For such reason, another recently developed NN called U-Net was chosen to accurately and effectively segment the defects on the surface of AM parts.

7.1 Application of PCA in feature identification

The main advantage of PCA is that it can reduce high-dimensional data sets to lower-dimensional data sets, thereby increasing the calculation speed. In actual research, according to the number of pixels within the sensitive area of the measuring instrument, the algorithm has to process a dataset which contains in excess of a million dimensions [110]. With such a big dataset and many dimensions of data to be coped with, the calculation speed will be significantly reduced. However, with the application of PCA, only the most crucial image parameters are to be calculated and processed during the measurement and the computational speed could be increased consequently [118].

7.1.1 Image parameter identification

In order to use PCA, the image parameters, or more widely used term features, are needed to be determined firstly. Such features are supposed to provide as much information of the image as possible while reducing the calculation time of the algorithm. For the purpose of making the sub-sectional images containing defects able to distinct from those without, 54 image parameters have been critically chosen and utilised in the PCA to represent the surface texture and surface topography of AM parts.

On the whole, the image parameters can be divided into 2 major categories: colour-related and texture-related parameters, in which 17 of them belong to colour-related type and the rest 37 amount to texture-related type. To provide greater detail about the acquisition of such image parameters, the colour-related ones were acquired through the computation of statistical parameters and the histogram entropies of 3 channel full colour images. Concurrently, the values of the texture-related parameters were worked out through computing the statistical parameters of blobs of images, binary local patterns and local edge

descriptors.

Achieving the calculation of the chosen image parameters, nearly 4 million dimensions of the dataset (taking into account the number of pixels in each image as well as the information stored in 3 different channels) can be largely reduced to just 54, which shortened the computing time for the algorithm to 233 seconds, making the processing much more efficient.

However, prior to calculating the parameters, another concern still needs to be taken into account. Albeit the image parameters were critically chosen, there is still a high probability that a great deal of redundant image related information is stored within those parameters, which would also potentially drag down the computational speed. To address such issue, a method called PCA fusion was employed to effectively fuse the features and thus further reduce the dimensions of image parameters. The retained new features are known to be the PCs, which are able to be restored the preserved image information from but also requires much less computation time for the algorithm. The principle of such method is described in-depth as below:

Considering a database consisting of n images, containing the ones with and without defects. As accounted above, each image can be represented by the m computed image parameters in an m × 1 vector where each parameter in the vector indicates the deviation from the mean value of the image parameters of n images.

7.1.2 Experiment on the basis of PCA

According to the working principle of PCA, a primary experiment was conducted based on the images captured by FV system. Firstly, the regular cubed Ti6Al4V AM sample with a representative top surface fabricated under the optimised settings was measured with Alicona G5 FV system under the magnification of 50× whilst the ring light was chosen to be the illumination source and the lateral and the vertical resolution were set to 1 μm and 50 nm. It can be viewed on the measuring results (Fig 7.1), the formerly accounted types of defects are nearly distributed on the top surface at random. In order to enable PCA to identify various types of defects from the non-defect areas on the top surface, the image was divided into 400 small segments, with 20 rows and 20 columns. Another purpose of this is to ensure that in most cases, only one obvious defect can be observed in each sub-sectional image, and the size

of these defects is comparable to the scale of the sub-sectional image. After splitting the original image, it was expected that images containing similar defects have similar image parameter values. In this pilot study, the segmental images with defects and no defects were manually labelled by experienced researcher and split into 2 datasets. Then the no defect set was set to be the training set and the defect set was set to be the testing set to investigate if PCA works fine for clustering the most visually different images. Then the image parameters of each image in the training set were calculated and established as the data matrix, the corresponding co-variance matrix, eigenvalues and eigenvectors could be computed accordingly following the previously described steps. The contribution and the cumulative contribution of each PC were calculated and listed in Table 7.1. As seen from the values of the cumulative contribution, the top 12 PCs have already covered all of the needed information. Thus only such PCs were retained and composed the 'filtered' defect matrix. In this particular case, the threshold for comparing the minimum norm distance between the projection of the defect images and the projection of the test images was set to 0.8. More specifically, only if the minimum norm distance between the defect and non-defect results is greater than 0.8 can the defect and non-defect images be separated successfully. However only fewer than 30% of the defect images can be categorised correctly which implies an unsuccessful application of PCA in such case study.

The reason for the inability of classifying the sub-sectional images into defect images and non-defect images accurately is complex. Firstly, the database is composed of grey scale images. Instead of using processed height maps of images, applying PCA to grey scale images directly improves the defect detection efficiency. However, these images which only include colour difference between peaks / hills and valleys / dales may not be able to represent the areal surface information of the measured area. Secondly, since the measured sample has a relatively smooth surface, the number of un-melted particles on the surface is limited and the size of them is essentially small, which makes differentiating the particles from the surface difficult. Additionally, the weld tracks in the background acting as background noise also make the defects on the surface less prominent.

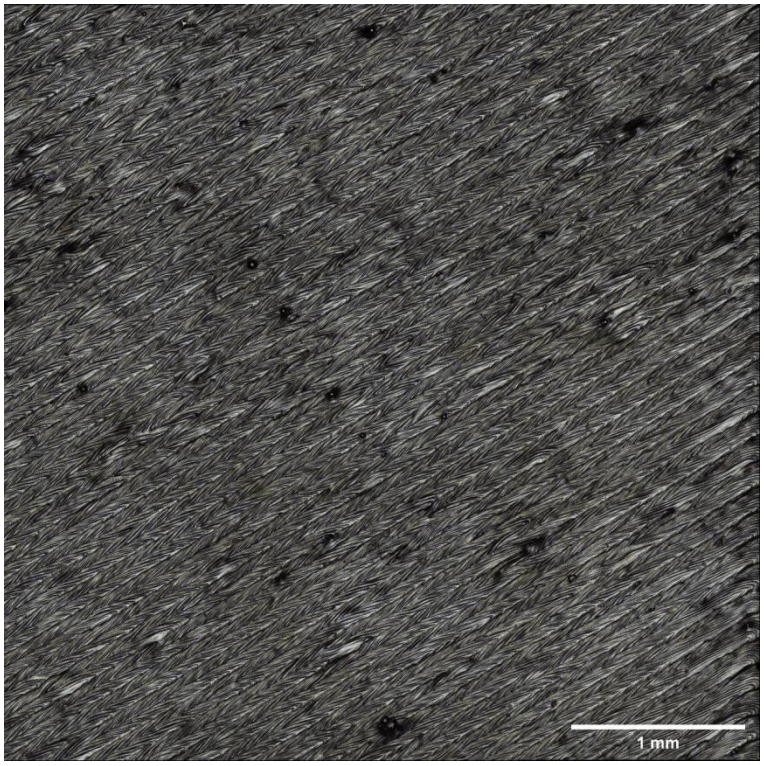

Fig 7.1 Top surface of Ti6Al4V part (sample 1) under FV

Table 7.1 Individual and cumulative contribution of each PC

Number of PC	Individual contribution of each PC	Cumulative contribution of each PC
1	0.7887	0.7887
2	0.1962	0.9850
3	0.0053	0.9903
4	0.0033	0.9936
5	0.0028	0.9964
6	0.0018	0.9983
7	0.0010	0.9993
8	4.6042×10^{-4}	0.9997
9	7.2061×10^{-5}	0.9998
10	6.0958×10^{-5}	0.9999
11	4.5788×10^{-5}	0.9999
12	3.6427×10^{-5}	1.0000
…	…	…

7.2 Application of CNN in feature identification

7.2.1 Convolutional neural network architecture

CNN is currently one of the most powerful ML techniques inspired by the working principle of visual cortex in the brain of human beings [119,120]. Its effectiveness in respect of pattern recognition, feature extraction, classification, verification and detection has been proven in a number of computer vision studies. A traditional classification CNN architecture consists of

three different types of layers, which are convolutional layer, pooling layer and fully connected layer.

7.2.1.1 Convolutional layer

Normally, within the standard convolutional layers, inputs are being filtered and combined to form new sets of output in a step. On the whole, a standard convolutional layer takes a D_F feature map $\boldsymbol{F}$ as an input and outputs a D_F feature map $\boldsymbol{G}$, where D_F denotes the width and height of a square input feature map, M denotes the number of input channels, D_G denotes the width and height of a square output feature map and N denotes the number of output channel. Such standard convolutional layer is then factorized by convolutional kernel **K** with a size of D_K where D_K denotes the dimension of the kernel. Accordingly the output feature map can be defined as:

$$\boldsymbol{G}_{k,l,n} = \sum_{i,j,m} \boldsymbol{K}_{i,j,m,n} \cdot \boldsymbol{F}_{k+i-1,l+j-1,m}$$

The computational cost of such standard convolution is in the form of:

$$D_K \cdot D_K \cdot M \cdot N \cdot D_F \cdot D_F$$

As aforementioned, the filtering and combining process of inputs are integrated in a single step in the standard convolution, however, this process could be enhanced with a CNN architecture named MobileNet with a massive reduction of the computation cost in the first few layers. Fundamentally, such architecture is based on depthwise separable convolutions which factorize the traditional convolution into a depthwise convolution and a 1 × 1 pointwise convolution. Fig 7.2 illustrates the architecture of depth separable convolution in comparison with standard convolution.

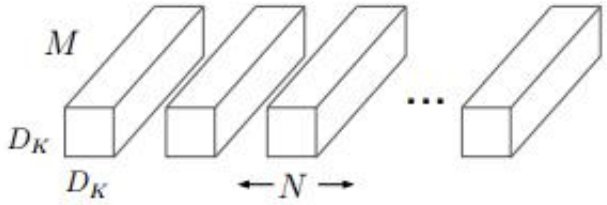

(a) Standard Convolution Filters

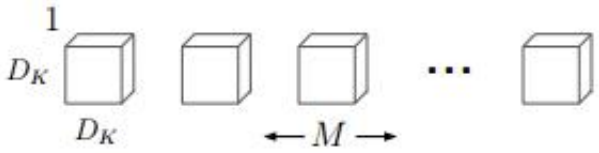

(b) Depthwise Convolutional Filters

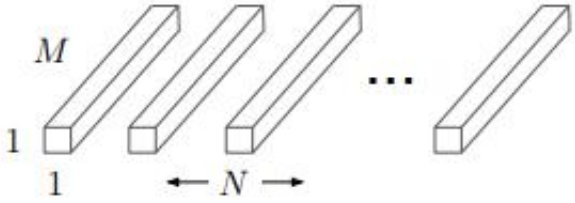

(c) 1×1 Convolutional Filters called Pointwise Convolution in the context of Depthwise Separable Convolution

Fig 7.2 Transformation from standard convolutional filter in (a) to the depthwise separable filter in (b) and (c) [121]

Within MobileNet, only a single filter is applied to each input channel, and then the outputs are unified with the application of pointwise convolution. Such sort of factorization is capable of achieving the reduction of computation cost as well as the size of the model. In addition, batchnorm in conjunction with Rectified linear unit nonlinearities are utilised for both described types of layers for the purpose of reducing the risk of gradient disappearance.

Concretely, the generic form of depthwise convolution with the application of one filter per input channel is:

$$\hat{\boldsymbol{G}}_{k,l,n} = \sum_{i,j} \hat{\boldsymbol{K}}_{i,j,m} \cdot \boldsymbol{F}_{k+i-1,l+j-1,m}$$

where $\hat{\boldsymbol{K}}$ denotes the depthwise convolutional kernel of size $D_{\boldsymbol{K}} \cdot D_{\boldsymbol{K}} \cdot M$ where the m_{th} channel of the filtered output feature map $\hat{\boldsymbol{G}}$ is generated when the m_{th} filter in $\hat{\boldsymbol{K}}$ is applied to the m_{th} channel in $\boldsymbol{F}$ and its computational cost is in the form of:

$$D_{\boldsymbol{K}} \cdot D_{\boldsymbol{K}} \cdot M \cdot D_{\boldsymbol{F}} \cdot D_{\boldsymbol{F}}$$

Albeit depthwise convolution is more efficient relative to standard convolution as the computational cost is reduced to 1/N of the original computational cost, new features cannot be generated with its use exclusively. Therefore, the pointwise convolution is used so as to compute and combine the outputs of depthwise convolutional layers and thus establish new features.

The summation of the described depthwise convolution and pointwise convolution is nominated as depthwise separable convolution, whose combined computational cost is in the form of:

$$D_K \cdot D_K \cdot M \cdot D_F \cdot D_F + M \cdot N \cdot D_F \cdot D_F$$

As a consequence, the reduction ratio of computational cost compared against the standard convolutional can be denoted as:

$$\frac{D_K \cdot D_K \cdot M \cdot D_F \cdot D_F + M \cdot N \cdot D_F \cdot D_F}{D_K \cdot D_K \cdot M \cdot N \cdot D_F \cdot D_F} = \frac{1}{N} + \frac{1}{D_K^2}$$

which indicates a massive increase in efficiency so that the recognition task can be carried out in a timely fashion.

In addition, within such NN, the Rectified Linear Unit [ReLU(z) = max (0, z)] [122] has been applied as the neuron activation function due to its good performance as regards computational time and its small generalisation error [123]. Also, the problem that the gradients decrease exponentially through the layers can be attended to with the use of such function.

7.2.1.2 Pooling layer

The pooling layer is where the feature maps are input and being resized into smaller segments. One of the most popular pooling layers is namely max-pooling layer, in which each map shrinks in the manner that the maximum value for a patch of 2 × 2 pixels. For the most part, it produces small invariance to translation and distortion, which results in a faster convergence and enhanced generalization.

7.2.1.3 Fully-connected layer

Fully-connected layers are usually located behind the convolutional layers and pooling layers. On the whole, they are in the form of a linear combination of input vector with its

corresponding weight matrix followed by a non-linear activation function [124]. Then the result can be indicated by the probability distribution in the form of an N-dimensional vector, in which N is the number of categories. The correlation in between high value features and possible clusters is established and the probabilities of each cluster are output accordingly.

7.2.2 Training process

Training is one of the most crucial steps within the supervised CNN. For the most part, deep CNN architecture, in this specific case the MobileNet, has millions of pre-set training parameters which normally determine its final performance. Concretely, the input images are mapped through the layers of the NN to output vectors. The training and test images are converted to vector pairs. Then the output error is obtained by computing the difference between the ground-truth output and the hypothesis. Categorical cross-entropy loss [125] has been commonly utilised for the evaluation of the output to achieve classification. Its form can be written as:

$$\text{Cost} = -\sum Y' \log(Y)$$

where Y and Y' are the hypothesis and the ground-truth value, respectively. Subsequently, the weights are gradually updated by backpropagation [126] for the purpose of finding the global optima of the cost.

7.2.3 Pre-processing

Due to the limitation of the number of measured AM surfaces, the database needs to be expanded to improve the training process. Because of such reason, the raw data of measured sample 1 and sample 2 were both split into 20 × 20 blocks, consistent with the manner of segmenting images for PCA application. In addition, the sizes of the blocks have been cut to 224 × 224 pixels per image for enhancement of the ML result. Furthermore, the grey values of the images have been adjusted from the standard range of 0 through 255 to the range of 0 through 1 for the purpose of normalisation. Within the pilot study of the application of CNN in defect identification, the images were categorised into 2 different types, and are labelled by experienced researchers as 'defect' and 'no-defect' respectively. Then the datasets were shuffled and split into a training set with 360 images (90% of the entire dataset) and a validation set with 40 images (10% of the entire dataset).

7.2.4 Overfitting tackling

Overfitting is one of the most widely concerned problems in ML where the overfitting of the data and hypothesis is normally caused by the use of overly large amount of features. It seems enhancing the match between the model and the database, however when new data comes into play, the classification / prediction results would become much less accurate. To attend to the problem, L2 regularisation with a λ of 0.01 as well as a dropout rate of 0.25 have been applied at this point to tackle the overfitting problem by not allowing model to rest on the outputs of one or a few neurons exclusively.

7.2.5 Results of model validation based on FV dataset

To investigate whether the model being chosen is suitable for resolving the defect classification problem, this section discusses the experiments of validating the MobileNet by altering its hyper-parameters based on the previously described FV database. The model with the corresponding parameters which provides a low computational cost as well as high recognition and validation accuracy is supposed to be uncovered after such tests. The computational cost for pre-training process indicates the execution time of training the selected database with the stored pre-trained parameters in MobileNet and the computational cost for validating process indicates how well the selected database is fitting the MobileNet. The dataset was divided into training set and validating set. Within this pilot investigation, two of the most crucial parameters which affect the recognition / validation accuracy, batch size and learning rate, were set to different values so as to discover the best settings. As the results in Fig 7.3 illustrate, the computational loss of the model for both pre-training as well as validating were regressed to below 1% in the cases of (a), (c), (d) and (f). However, whilst the batch size amounts to 25, the computational loss for both pre-training and validating fluctuates within such period and not regressed at the end of the iterations. Normally the reason for this relatively poor performance is the learning rate was not appropriately selected, which yields a so-called overshooting where the computational cost is not able to reach the global optima. It is also worth noting that whilst the learning rate amounts to 10^{-3}, batch size amounts to 9, the recognition rate of validation set is only 8.8%. Nonetheless, within the rest of the sets of the training parameters, the recognition accuracy of validation set can get above 90% stably as shown in Table 7.2, which proved the MobileNet is suitable for defect

detection based on the FV database.

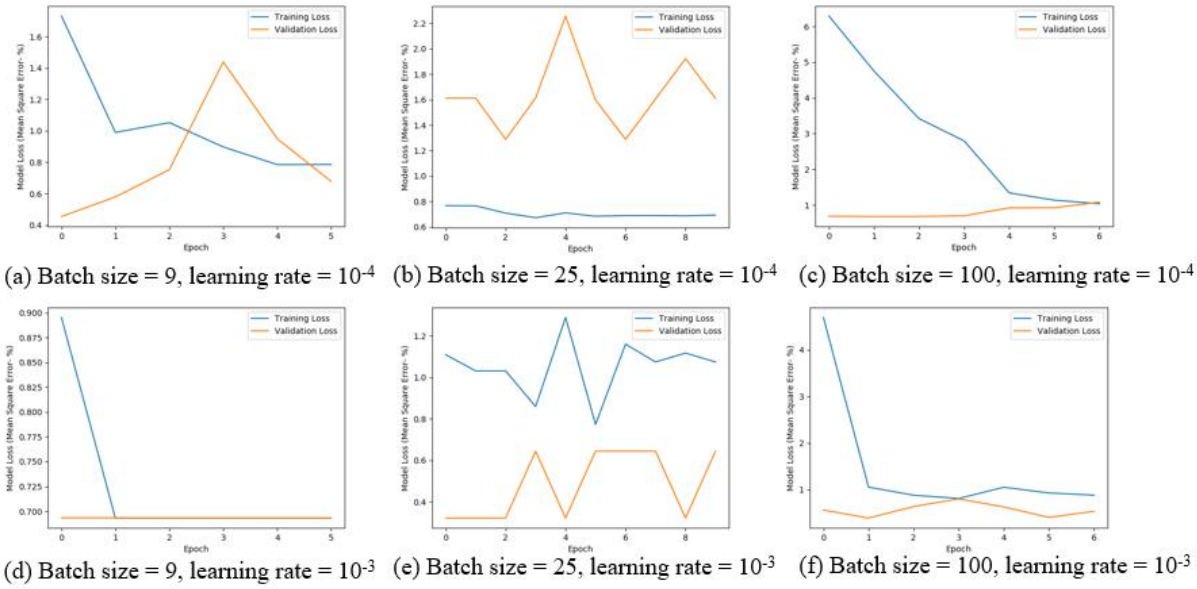

(a) Batch size = 9, learning rate = 10^{-4} (b) Batch size = 25, learning rate = 10^{-4} (c) Batch size = 100, learning rate = 10^{-4}

(d) Batch size = 9, learning rate = 10^{-3} (e) Batch size = 25, learning rate = 10^{-3} (f) Batch size = 100, learning rate = 10^{-3}

Fig 7.3 Computational costs of both training and validating whilst different training parameters being selected (FV)

Table 7.2 Recognition rates of the machine in different learning rates and batch sizes (L = learning rate, BS = batch size)

L (%) \ BS	9	25	100
10^{-4}	91	90	91
10^{-3}	8.8	96	95

7.2.6 Results of model validation based on fringe projection dataset

In this section, the investigation into the classification validity of MobileNet based on the previously acquired FP data of sample 2 has been carried out as well. Similarly, the dataset has been split into the training and validating sets, and the sizes of the blocks have been cut to 56 × 56 pixel per image to enhance ML. Fig 7.4 demonstrates the orthogonal test results with the alteration of learning rate and batch size. As it can be seen from the graphs, (b), with a batch size of 25 and learning rate of 10^{-4}, gives the besting fitting results where the computational losses for both learning and validating processes were regressed to below 1%, whereas (c) and (d) were still potentially affected by the overfitting problem, which can be seen from the fluctuations in the graphs. Table 7.3 shows the recognition accuracy based on the FP is also able to achieve up to 96% when the trained parameters were well tuned, which proves the suitability of defect detection with the use of MobileNet based on the FP data.

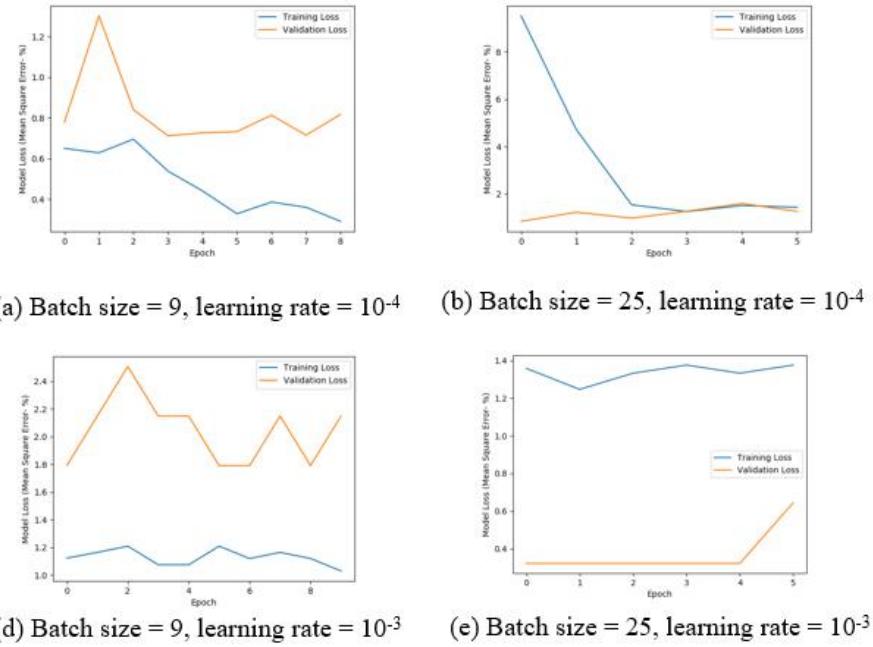

(a) Batch size = 9, learning rate = 10^{-4} (b) Batch size = 25, learning rate = 10^{-4}

(d) Batch size = 9, learning rate = 10^{-3} (e) Batch size = 25, learning rate = 10^{-3}

Fig 7.4 Computational costs of both training and validating whilst different training parameters being selected (FP)

Table 7.3 Recognition rates of the machine in different learning rates and batch sizes (L = learning rate, BS = batch size)

L (%) \ BS	9	25
10^{-4}	80	92
10^{-3}	86.67	96

7.3 Application of U-Net in defect segmentation

7.3.1 Architecture

Aside from CNN, there is another deep learning framework for feature extraction that image segmentation algorithms are based on, named as full convolutional network (FCN). The former is prone to detail loss of images in the process of convolving and pooling, and the method of using the fully connected layer to obtain the category probability results in the inability to identify each pixel category, so accurate segmentation cannot be achieved; while in the latter framework, fully connected layers are replaced by convolutional layers. Up-sampling is added prior to pooling operations to resolve the problem of accurate segmentation, however it does not have a good performance in the edge extraction.

On the basis of FCN network, U-net was developed [127]. The network architecture includes

two symmetrical parts: a contraction path and an expansion path: the contraction path has a similar appearance to the ordinary convolutional network, down-sampling the segments with the use of 3×3 filters in the process of convolving and pooling to obtain the shallow features (the features extracted in the early convolutions) and deep features (the features extracted in the later convolutions, acquiring the relevance between pixels; the expanded path is essentially symmetrical with the contracted path, using 3×3 filters in the process of convolving followed by up-sampling layers, and the shallow and deep features are combined during the process of up-sampling. As a result, the image is able to be segmented in an accurate manner. This feature fusion operation makes full use of the shallow and deep features in the image to achieve better segmentation results (Figure 7.5).

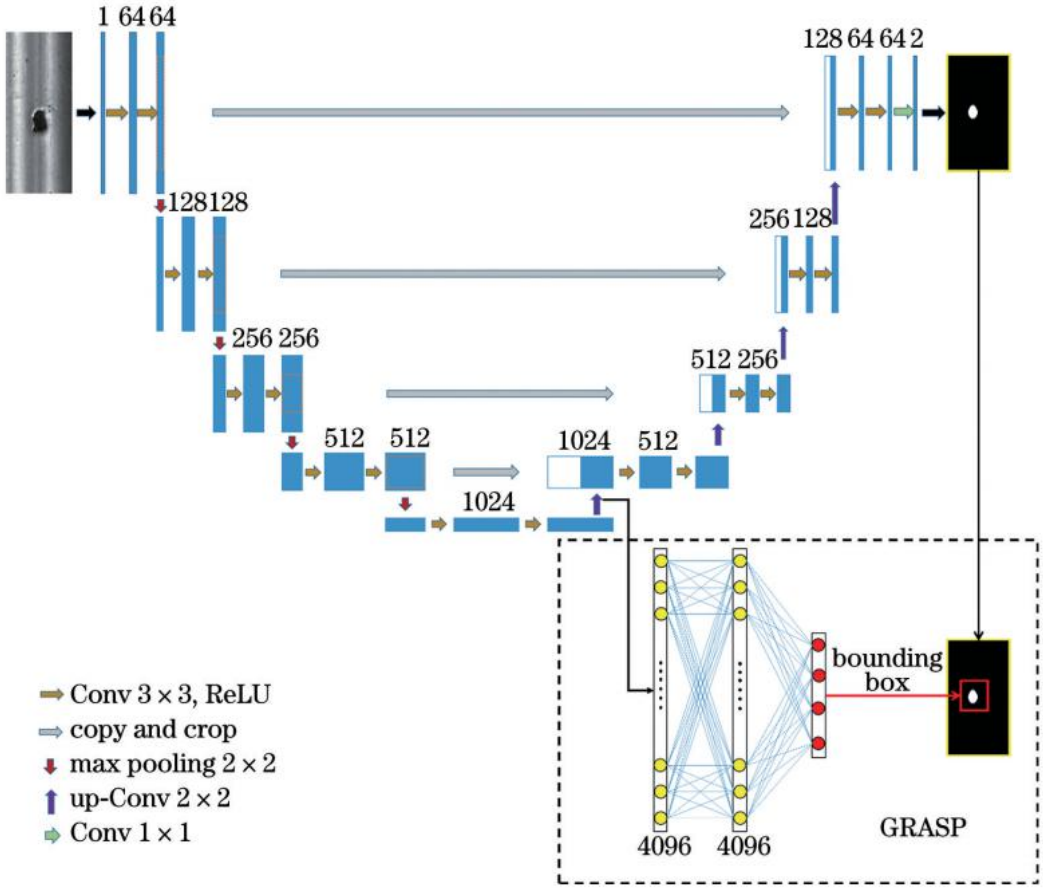

Fig 7.5 Architecture of U-Net [127]

7.3.2 Model framework and parameter settings

The setting of the hyper-parameters of the model affects the performance of the network. The U-Net model was built using the Python framework. Parameter setting was set as: the training

batch size is 100, the learning rate is 10×10^{-5}, and the target size is 50×50.

7.3.3 Training optimisation

In order to obtain more high-resolution information, batch normalisation was performed after each convolution to avoid gradient dispersion to improve the generalisation ability of the model. It could also allow the learning rate to be higher to accelerate the convergence. Also similarly to the lost function used in MobileNet, binary cross-entropy loss function was used since the computational loss will be close to infinite if the prediction is confident but false, which improved the stability of the computational loss.

7.3.4 Overfitting tackling

As previously mentioned, as one of the most widely concerned problems in ML, overfitting of the data and hypothesis is normally caused by the use of overly large amount of features. To tackle this problem in the model of U-Net, the input images were normalised to eliminate the influence of other functions on the image transformation. A dropout mechanism was added to the NN. Dropout refers to the temporary inactivation of neural units from the network with a certain probability during the training process.

7.3.5 Results of model training and validation

Two regions of interest with an area of 10 mm × 10 mm on sample 3 were chosen at random. Then the regions were measured by FV and used as the training set and testing set. The training image was split into sub-sections and the random rotation and flipping of images were applied to those sub-sections to augment the dataset. The size of the sub-sections have been set to 568 × 568 pixels per image for enhancement of the ML result. The Fig 7.5 and Fig 7.6 showed the original processed measured image prior to image transformation and the corresponding labelled image. Firstly, the images was trained by the U-Net model. Then, in order to examine the performance of U-Net in segmenting the image to achieve defect detection, the test image (Fig 7.7) was input to the model for validation. The training loss, training accuracy, validation loss and validation accuracy are listed in Table 7.4. The validation loss was even slightly smaller compared to the training loss. This demonstrated a good validation performance, despite the fact the accuracies of training and validation were

equivalent. The segmented result is shown in Fig 7.8. As briefly mentioned above, since the added up-sampling prior to pooling operations is not good at extracting the edges of the image, blurry edges and detail loss can be discovered in both of training and validation images.

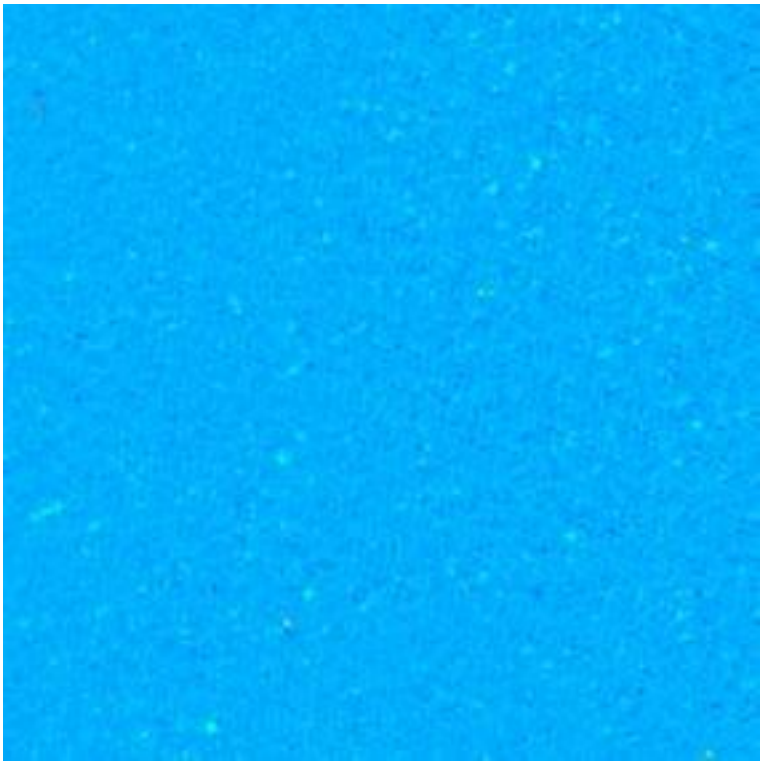

Fig 7.5 Processed measured image of a random region on sample 3

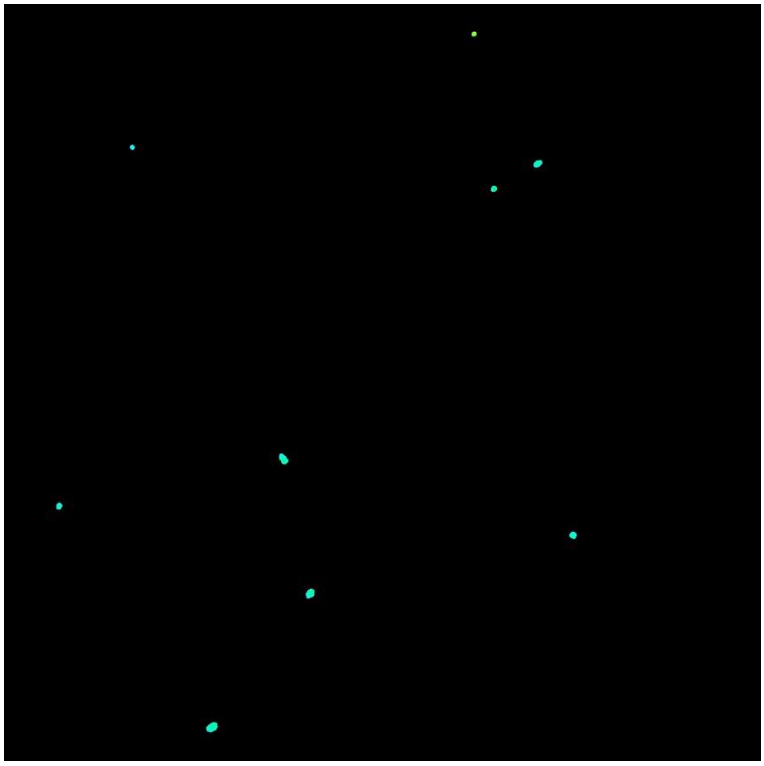

Fig 7.6 Labelled processed measured image of a random region on sample 3

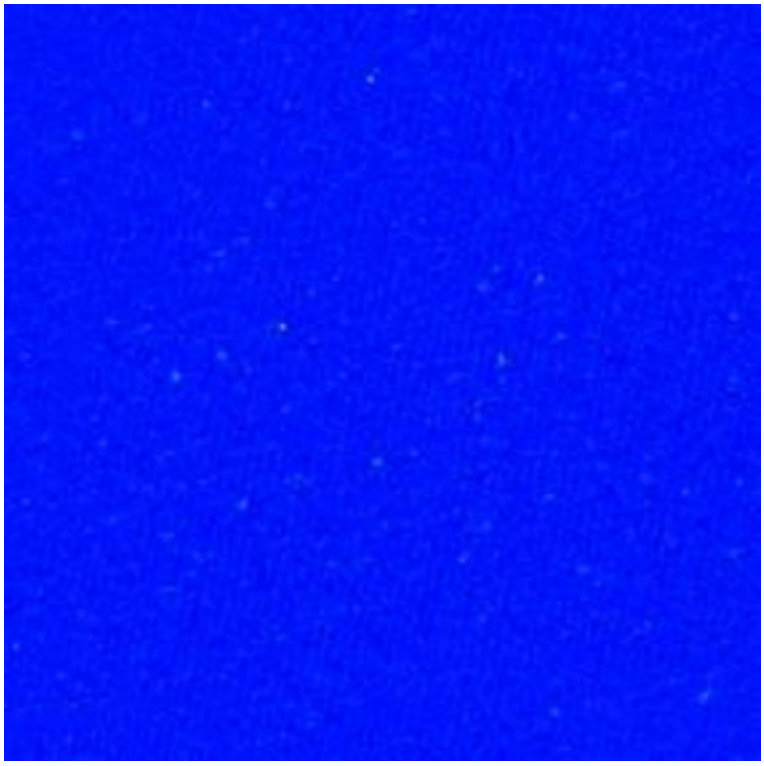

Fig 7.7 Input test processed measured image of a different region on sample 3

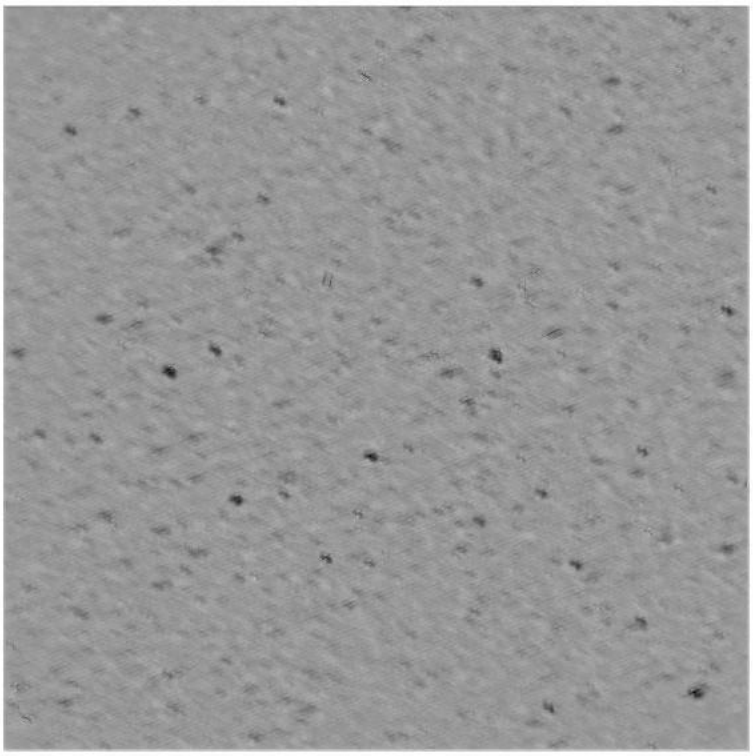

Fig 7.8 Test image after defect segmentation

Table 7.4 Computational loss and accuracy of both training and validation

	Computational loss	Accuracy
Training	0.0026	0.9998
Validation	0.0033	0.9998

8. Discussion

8.1 Overview of the research methodology

Basic scientific research rules were followed within the research methodology:

1) The samples with different materials and sizes extensively provided most sorts of frequently discovered defects in AM and provided various sources of data for the following defect detection tasks;

2) The samples were then measured by high precision optical measuring techniques including FV and FP to secure the accuracy of data;

3) Following the measurements, the optimal filtration method was determined and used to process the measured surface to ensure the correctness of the dataset;

4) In comparison with traditional digital image processing method which is difficult to extract irregular defect patterns and to apply in real time, this thesis used ML to achieve the objective of defect detection, which is more effectively and efficiently able to determine features with complex geometries without the use of advanced thresholding techniques;

Nonetheless, the research methodology can still be improved in the following manners:

1) There may not be many complex structures on the surface of well fabricated AM parts and certain materials of samples are translucent and reflective. For this reason, FV is no longer suitable for measuring the surface under this circumstance. Albeit FP is another method for measuring features with hundreds of microns, because of the relatively long working distance, it is difficult to obtain the detailed geometry of the defect;

2) Although it is useful to determine the boundaries of defects on the surface using the optimal filtration method as a manner of pre-processing the data, the computation of the contours is still time consuming and the filtered results may not fully represent the true information of features;

3) The drawbacks of ML methods remain, for instance, it is time consuming to acquire and establish a very informative dataset for the ML method to be trained with, and requires very high-specification CPU and huge memory for computation;

8.2 The advantages and disadvantages of the used ML methods

As discussed above, ML has various advantages in the application of defect detection for AM parts. Because: unlike traditional digital image processing in which advanced thresholding techniques need to be used, ML is capable of identifying complex geometries implicitly; it is also more effective in detecting defects on the condition that the training dataset is well established, as a result it is much more time and energy saving. Furthermore, it is able to cope with changing data yielded in the fluctuating manufacturing process by training the model. However, in order to achieve a high feature recognition rate, the dataset needs to contain a large amount of information to be trained with. Additionally, since the training process is running depending on thousands of instances and the information stored in the millions of neurons in the model is renewed in real time in the training process, a very high-specification CPU and huge memory are necessary for computation.

8.2.1 PCA

Since the number of pixels within the sensitive area of the measuring instrument in this thesis is larger than 4 million, the ML algorithm has to cope with a dataset which contains the same amount of dimensions. As a typical unsupervised ML method, PCA is capable of reducing high-dimensional datasets to lower-dimensional datasets by only calculating the most critical image parameters to significantly increase the computational speed. In this thesis, nearly 4 million dimensions of the dataset was reduced to just 54, which cut the computing time to 233 seconds, thus increasing the efficiency of the computation.

Nevertheless, as aforementioned, grey scale images that only contain colour difference between high points and low points was not fully able to be representative of the areal surface information of the measured area. Since PCA is applied based on statistics, the infrequent presence of defects on finely fabricated AM surfaces made the classification difficult. In addition, it is also difficult for PCA to address the negative impact of the background noise (in this case weld tracks) to the classification task.

8.2.2 CNN (MobileNet)

CNN is one of the most powerful ML methods at present and it has been proven effective in achieving pattern recognition, feature extraction, classification, verification and detection in

computer vision studies. As one powerful sort of CNNs, MobileNet was able to further reduce the computation cost and shrink the size of the model, in which: the convolutional layers can largely increase the efficiency with the application of pointwise convolution, the pooling layers provide faster convergence and enhanced generalisation, the fully-connected layers output the probability distribution as the classification result.

However, as previously mentioned, overfitting is one of the most widely concerned problems specifically in CNN. One of the objectives of ML is to enhance the match between the ML model and the database correctly to produce accurate prediction results. However, when new data to the model appear, due to the existence of overfitting of the data and hypothesis, the classification / prediction accuracy would decrease provided the number of features is too huge. In addition, it is prone to detail loss of images in the process of convolving and pooling, and the accurate segmentation cannot be achieved as the method of using the fully connected layer to obtain the category probability is not able to identify each pixel category.

8.2.3 U-Net

Different from CNN, U-Net uses convolutional layers instead of fully connected layers and uses up-sampling operation to achieve accurate defect segmentation so the full information including size and geometry of defects is acquired. Furthermore, batch normalisation improves the generalisation ability of the model and accelerates the convergence.

Same as for CNN, overfitting is also a major problem for U-Net. This problem may be tackled considerably by normalising the input images to reduce the impact of other functions on the image transformation. Additionally, the edges of the image is difficult to be extracted when using U-Net, blurry edges were yielded and there was a loss in details as a result.

9. Conclusions

9.1 Thesis summary

The ultimate aim of the thesis was to develop effective defect detection methods for AM parts with the application of different ML techniques.

The first objective of the thesis was to determine the optimal instrument settings and good practice for the measurement of surface topography of additive surfaces using FV - addressed in Chapter 4. The second objective of the thesis was to compare different typical filtration methods, including Gaussian filters and morphological filters, and determine the most suitable filtering method for characterising the defect features on the surface of AM parts - addressed in Chapter 5. The final objective of the thesis was to investigate both unsupervised learning and supervised learning methods to examine their applicability of image classification and image segmentation, and eventually achieve the defect detection for AM parts - addressed in Chapter 6.

Since the work in this thesis focused mostly on the practice of being able to detect the defects on AM parts, it is critical to understand the detailed information about different sorts of defects firstly. The defect review in Chapter 2 aims to collect the information in terms of the defects in LPBF process based on the related research of the global researchers. Firstly, the mostly discovered types of defects are successively classified by their ordinary appearances. Then more detailed information with respect to each sort of defects has been discussed in the manner of their morphologies, major causes and possible negative effect on the density of the parts. Subsequently, an effort has been made on attempting to identify the connection among the different types of defects and other factors. The contribution of this review chapter is that it provides the details about different types of defects and discusses the potential correlation between process parameters and generated defects. Having understood the morphologies of the defects can provide the researchers a practical guideline for choosing the appropriate metrology and measurement instrument to inspect the defects, e.g. using high resolution measurement instrument to measure micro scale defects. An understanding of the relevance between process parameters and defects is also required to help further avoid defect

generation. Chapter 3 introduced the overall research route in this article. Firstly, the samples in different shapes and materials to be measured were introduced briefly. Then the two selected optical metrology instruments for measuring AM surfaces, which are FV and FP, and their working principles were explained in detail. In addition, a comparison of several classic filtration methods was carried out to determine the method with the best filtering effect for the AM surface. Finally, different ML methods were applied to achieve the ultimate goal of defect detection. With the design of such research methodology, the aims and objectives of this thesis can be fulfilled with the measurement of AM parts with the optimised instrument settings, the appropriate pre-processing (surface filtration) and the defect classification and segmentation.

ML and AM are both research fields that have developed rapidly in recent decades. In particular, the combination of the two can effectively achieve the purpose of AM parameter optimisation, process control and defect detection. Therefore, Chapter 4 reviewed the adaptability of ML to different types of data and its application in feature extraction to achieve in-line or offline defect detection. This review is a contribution that summarises the ML application for defect detection in AM. Specifically, it demonstrated how to select proper ML technique given various types of data and how to choose appropriate ML model depending on different forms of defect detection (defect classification and defect segmentation).

In order to provide accurate and reliable data for the subsequent feature extraction and defect detection, it is necessary to explore the optimal measurement settings of optical metrology instruments initially. Chapter 5 optimised the parameters including the magnification of objective lens and illumination source of the optical instrument. By selecting the highest magnification of the optical instrument for acquiring more details, selecting the ring light for relatively rough AM surface and using the recommended lateral and vertical resolution suggested by the measurement software, Chapter 5 contributed high-confidence measurement results and provided a good practice for such measurement.

In general, the measured AM surface can be further divided into waviness component and roughness component. Since the defects and features that have the greatest impact on the

quality of parts are with micron scales, in order to facilitate the recognition of such features on the surface, waviness component on the order of millimeters was disregarded in this thesis. Then, Chapter 6 compared several different classic filtration methods to discover the best filtering method for AM surfaces. Finally, according to the characteristics of AM surface topography, the 'opening + closing' morphological filter had the best performance, and the filtered measurement results also provided a reliable data source for subsequent defect detection with the use of ML. As such, this chapter can be considered a valuable guideline to pre-process and filter the as-measured AM surface for either characterising the surface topography of AM parts or more importantly for this work, generating refined height maps for following ML.

In Chapter 7, the applicability of different types of machine learning methods for defect detection was investigated. Machine learning can be basically divided into unsupervised learning and supervised learning. As a representative method of unsupervised learning, PCA has a stable performance in feature extraction. However, although the method of only retaining the PC greatly improved the learning efficiency, the experiment showed that in this case, PCA did not successfully distinguish the surface defect from the defect-free area. As such, the experiment in this work is a contribution to the application of PCA to the defect detection for LPBF surface which demonstrated that due to the small size of particles, the form of measured images (grey scale images) and the complex texture of LPBF surfaces including weld tracks acting as background noise, PCA may not be a suitable tool for classifying defects if using exclusively.As for supervised learning, this thesis discussed two CNN-based models: MobileNet and U-Net, where the former is mostly used for classification tasks, and the latter can be used for direct image segmentation. By selecting an appropriate model depending on the purpose of ML (defect classification or segmentation), pre-processing the measured results from the last chapter to make them more suitable for ML, tuning the hyperparameters of the model to improve its accuracy and efficiency, this chapter contributed two tuned and modified ML models which have good performance in correctly classifying defects and segmenting defects from the measured surface.

Chapter 8 summarised the proposed research methodology, including the choice of samples,

measurements of the samples, filtration method optimisation and the investigation of ML methods. It also revealed there are still aspects that the research methodology can be improved on. Additionally, it discussed the 3 different ML methods that were proposed and implemented in this thesis in detail, and what their advantages and disadvantages are in the application of defect detection.

9.2 Contributions to the research field

The main contribution are summarised by Chapter as follows, including key findings and observations of this work.

For Chapter 2 which reviewed different types of defects in LPBF, the key findings and observations relative to the aims and objectives were:

1) When a defect is combined by multiple defects, it is suggested classifying it into an independent type of defect;

2) However, defects are still mainly categorised into pores, cracks, balling behaviour, un-melted particles, pits, scratches and deformation. Many factors can be correlated to the generation of such defects, including scanning strategy, building orientation, laser energy input, powder mass, powder density, powder arrangement, gas flow and surface tension;

3) Due to the correlation between signatures and the corresponding process parameters that affect them, the study of signatures was taken into consideration as an alternative to directly monitoring the defects, which can dynamically adjust the process parameters to avoid further defects;

4) Regarding the negative impact defects have on the quality of AM parts, a defect with size up to 200 μm will yield loose parts whereas a defect with size up to 500 μm can lead to failed parts;

5) There are a variety of measurement / metrology techniques to measure AM samples. The results have forms depending on the sensors being used. However, optical measurement was preferred as it can provide the real areal surface topography with high image resolution. Furthermore, the measurement is recommended being carried out at the original building

position wherever possible.

Chapter 3 presented a methodology to achieve the defect detection which contributed a novel research route including sample measurement with FV and FP under the optimal instrument settings, data processing and preparation in which the optimum filtration method for this field is determined, and the determination of appropriate ML methods and their parameters to achieve accurate defect detection (defect classification and defect segmentation). It is critical that optical instrument FV and FP were used in the experiments as they are able to provide the real areal surface topography of AM parts. Following this route, the aims and objectives of this thesis can be successfully achieved.

For Chapter 4 which reviewed different ML applications for defect detection in LPBF, the key findings and observations relative to the aims and objectives were:

1) There are various ways of capturing data of AM parts, e.g. the inspection can occur either in-line or offline, the metrology instrument can either be embedded within or outside the manufacturing chamber, and the data can be collected by different types of sensors. However, obstacles in terms of measurement environment, measurement accuracy, measurement efficiency exist in such inspection manners;

2) Among the ML methods which are commonly used in the field of defect detection for AM parts, PCA as an unsupervised learning method that is good at coping with high dimensional data can be used for defect classification, and NN as a supervised ML technique can be used for its proven high reliability and advanced function (defect segmentation).

For Chapter 5, which discussed the sample measurement of AM parts, a practical guide for optimising the measurement instrument settings is:

1) Initially, it is critical to select the correct objective lens for the measurement. Since the surface defects normally distribute in relatively small region of interest, the highest magnification of objective lens (50×) was chosen to acquire more details;

2) Since the AM surface is not smooth mostly, It is recommended that the ring light be chosen for AM surfaces to improve the lighting condition;

3) Vertical resolution should be minimised within the recommended range to stabilise the measurement result, however it may incur an excessive measurement time;

4) Lateral resolution should also be minimised within the recommended range by the instrument software. Nonetheless, it should not be set too close to the lower limit to avoid inducing more high frequency noise on the surface;

Chapter 6 presented a method to prepare the database for ML, including generating the height map with the selection of appropriate surface filtration method and data augmentation. The findings of this chapter were:

1) It was suggested that the 'opening + closing' morphological filter had the best performance in surface filtration for generating height map incorporating the surface defect information as it can enhance the peaks/hills and suppress the valleys/dales;

2) The use of data augmentation including random rotation, translation, flipping of images were able to tackle the problem of lacking data. By doing this the size of the dataset was expanded and the overfitting was reduced simultaneously.

Chapter 7 contributed a series of case studies investigating different ML applications for defect detection in AM. The key findings of this chapter were:

1) PCA is able to greatly reduce the computational time since the dimensions of image were reduced from 4 million to 54;

2) Furthermore, by establishing the co-variance matrix, the dimensions of each sample can be further reduced to 12 by only retaining the PCs;

3) For classification CNN MobileNet, the overfitting problem can be successfully addressed using L2 regularisation and drop out;

4) A high recognition rate up to 96% can be achieved when the hyperparameters of the model were well adjusted (e.g. batch size = 25, learning rate = 10^{-3});

5) For U-Net, drop out can be applied to tackle the overfitting as well;

6) U-Net was capable of segmenting the defects in the test image when the labelled data was

well learnt, and the validation accuracy can reach 0.9998;

Chapter 8 briefly recapitalized the used research methodology in the thesis, and demonstrated that it is effective to achieve the objective of defect detection. It also pointed out the weaknesses of the used research methods. Then the suitability of three different ML methods, including PCA, CNN and U-Net in defect detection was discussed. It was proven that the proposed ML methods had good performances in achieving defect detection. However, it also emphasized the drawbacks the methods had in the application of defect detection and attempted to provide solutions.

9.3 Areas for future work

There are still a variety of areas of future work that can be conducted to further the aims and objectives of this thesis.

Regarding Chapters 3, more measurement instruments which can potentially achieve efficient and accurate metrology can be considered being developed and used in future work. The samples measured in this work all have regular geometries and the measured surface is perpendicular to the building orientation. As aforementioned, some defects can be attributed to an inappropriate building location and orientation. As such, in the future research, the variety of samples needs to be increased to provide more types of surface topographies. Additionally, if the to-be-fabricated samples have smoother surfaces, then it requires re-determining the illumination source for optimum lighting condition.

For Chapter 6, the reason why the ‘opening + closing’ filtration method was selected is un-melted particles were the typical and dominant feature on the surface of AM samples, and such filter is capable of enhancing peaks/hills (un-melted particles) and suppressing valleys/dales. However, if the dominant features on the surface of to-be-fabricated AM parts have changed in the future work, e.g. pores, then a more suitable filtration method that is able to cope with the new surface topography needs to be determined. In addition, only random rotation and flipping of images were used to augment the dataset. In future work, more image transformations can be chosen to discover how this operation will affect the training process.

In respect of Chapter 7, future work can focus on how to improve the applicability of PCA in

defect classification for AM parts. In this work, only the grey values of images were normalised as a way of pre-processing data for PCA. An experiment can be designed to determine whether applying filters to the normalised image can improve the classification accuracy of PCA in the future work. For NN, more values of hyperparameters and number of parameters can be used in the future orthogonal array testing experiment to further improve the suitability of the model for the training data. Lastly, the L2 regularisation and drop out were applied with their default values in this thesis, such values can be attempted tuning in the future work to better attend to overfitting problems.

For Chapter 8, As aforementioned, regarding the drawbacks of the proposed research methodology, more advanced and suitable measuring instruments are needed to capture the detailed information of AM surfaces. More manual work instead of filtering methods can be used to process the data in order to reduce data preparation time. How to achieve an accurate defect detection with sparse data can also be researched on as this can save much computational power.

In terms of the ML methods, for PCA, real surface data as opposed to grey scale images can be used in PCA to represent the true information of the AM surface. More advanced methods which can remove weld tracks on surface images is also required for a better classification result. For both CNN and U-Net, overfitting problems still need to be better tackled with the use of different sorts of normalisation.For U-Net, a better architecture of the network needs to be designed to avoid the blurry edges and detail loss in the image.

References

[1] ASTM International, “F2792-12a - Standard Terminology for Additive Manufacturing Technologies,” Rapid Manuf. Assoc., pp. 10–12, 2013, doi: 10.1520/F2792-12A.2.

[2] I. Gibson, D. Rosen, and B. (Brent) Stucker, Additive manufacturing technologies : 3D printing, rapid prototyping, and direct digital manufacturing. .

[3] F. Helmli, “Focus Variation Instruments,” in Optical Measurement of Surface Topography, 2011.

[4] I. Maskery et al., “Quantification and characterisation of porosity in selectively laser melted Al-Si10-Mg using X-ray computed tomography,” Mater. Charact., 2016, doi: 10.1016/j.matchar.2015.12.001.

[5] H. Gong, K. Rafi, H. Gu, G. D. Janaki Ram, T. Starr, and B. Stucker, “Influence of defects on mechanical properties of Ti-6Al-4V components produced by selective laser melting and electron beam melting,” Mater. Des., vol. 86, pp. 545–554, 2015, doi: 10.1016/j.matdes.2015.07.147.

[6] H. Gong, K. Rafi, H. Gu, T. Starr, and B. Stucker, “Analysis of defect generation in Ti-6Al-4V parts made using powder bed fusion additive manufacturing processes,” Addit. Manuf., vol. 1, pp. 87–98, 2014, doi: 10.1016/j.addma.2014.08.002.

[7] C. Weingarten, D. Buchbinder, N. Pirch, W. Meiners, K. Wissenbach, and R. Poprawe, “Formation and reduction of hydrogen porosity during selective laser melting of AlSi10Mg,” J. Mater. Process. Technol., vol. 221, pp. 112–120, 2015, doi: 10.1016/j.jmatprotec.2015.02.013.

[8] J. Schwerdtfeger, R. F. Singer, and C. Körner, “In situ flaw detection by IR‐imaging during electron beam melting,” Rapid Prototyp. J., vol. 18, no. 4, pp. 259–263, Jun. 2012, doi: 10.1108/13552541211231572.

[9] S. A. Khairallah, A. T. Anderson, A. Rubenchik, and W. E. King, “Laser powder-bed fusion additive manufacturing: Physics of complex melt flow and formation mechanisms of pores, spatter, and denudation zones,” Acta Mater., vol. 108, pp. 36–45, 2016, doi: 10.1016/j.actamat.2016.02.014.

[10] R. Engeli, T. Etter, S. Hövel, and K. Wegener, “Processability of different IN738LC powder batches by selective laser melting,” J. Mater. Process. Technol., vol. 229, pp. 484–491, Mar. 2016, doi: 10.1016/J.JMATPROTEC.2015.09.046.

[11] S. Tammas-Williams, H. Zhao, F. Léonard, F. Derguti, I. Todd, and P. B. Prangnell, “XCT analysis of the influence of melt strategies on defect population in Ti–6Al–4V components manufactured by Selective Electron Beam Melting,” Mater. Charact., vol.

102, pp. 47–61, Apr. 2015, doi: 10.1016/J.MATCHAR.2015.02.008.

[12] A. J. Sterling, B. Torries, N. Shamsaei, S. M. Thompson, and D. W. Seely, “Fatigue behavior and failure mechanisms of direct laser deposited Ti-6Al-4V,” Mater. Sci. Eng. A, vol. 655, pp. 100–112, 2016, doi: 10.1016/j.msea.2015.12.026.

[13] E. Wycisk, A. Solbach, S. Siddique, D. Herzog, F. Walther, and C. Emmelmann, “Effects of Defects in Laser Additive Manufactured Ti-6Al-4V on Fatigue Properties,” Phys. Procedia, vol. 56, pp. 371–378, Jan. 2014, doi: 10.1016/J.PHPRO.2014.08.120.

[14] X. Zhao et al., “Comparison of the microstructures and mechanical properties of Ti-6Al-4V fabricated by selective laser melting and electron beam melting,” Mater. Des., vol. 95, pp. 21–31, 2016, doi: 10.1016/j.matdes.2015.12.135.

[15] N. T. Aboulkhair, N. M. Everitt, I. Ashcroft, and C. Tuck, “Reducing porosity in AlSi10Mg parts processed by selective laser melting,” Addit. Manuf., vol. 1–4, pp. 77–86, Oct. 2014, doi: 10.1016/J.ADDMA.2014.08.001.

[16] I. Yadroitsev, P. Krakhmalev, and I. Yadroitsava, “Hierarchical design principles of selective laser melting for high quality metallic objects,” Addit. Manuf., vol. 7, no. December, pp. 45–56, 2015, doi: 10.1016/j.addma.2014.12.007.

[17] Y. J. Liu et al., “Microstructure, defects and mechanical behavior of beta-type titanium porous structures manufactured by electron beam melting and selective laser melting,” Acta Mater., vol. 113, pp. 56–67, 2016, doi: 10.1016/j.actamat.2016.04.029.

[18] L. Thijs, F. Verhaeghe, T. Craeghs, J. Van Humbeeck, and J.-P. P. Kruth, “A study of the microstructural evolution during selective laser melting of Ti-6Al-4V,” Acta Mater., vol. 58, no. 9, pp. 3303–3312, May 2010, doi: 10.1016/j.actamat.2010.02.004.

[19] K. Monroy, J. Delgado, and J. Ciurana, “Study of the Pore Formation on CoCrMo Alloys by Selective Laser Melting Manufacturing Process,” Procedia Eng., vol. 63, pp. 361–369, Jan. 2013, doi: 10.1016/J.PROENG.2013.08.227.

[20] C. Kong, C. J. Tuck, I. a. Ashcroft, R. D. Wildman, and R. Hague, “High Density

Ti6Al4V Via Slm Processing: Microstructure and Mechanical Properties," Solid Free. Fabr., 2011.

[21] K. Darvish, Z. W. Chen, and T. Pasang, "Reducing lack of fusion during selective laser melting of CoCrMo alloy: Effect of laser power on geometrical features of tracks," Mater. Des., vol. 112, pp. 357–366, 2016, doi: 10.1016/j.matdes.2016.09.086.

[22] I. Yadroitsev, L. Thivillon, P. Bertrand, and I. Smurov, "Strategy of manufacturing components with designed internal structure by selective laser melting of metallic powder," Appl. Surf. Sci., vol. 254, no. 4, pp. 980–983, Dec. 2007, doi: 10.1016/J.APSUSC.2007.08.046.

[23] B. Baufeld, E. Brandl, and O. van der Biest, "Wire based additive layer manufacturing: Comparison of microstructure and mechanical properties of Ti–6Al–4V components fabricated by laser-beam deposition and shaped metal deposition," J. Mater. Process. Technol., vol. 211, no. 6, pp. 1146–1158, Jun. 2011, doi: 10.1016/J.JMATPROTEC.2011.01.018.

[24] J. Günther et al., "Fatigue life of additively manufactured Ti–6Al–4V in the very high cycle fatigue regime," Int. J. Fatigue, vol. 94, pp. 236–245, 2017, doi: 10.1016/j.ijfatigue.2016.05.018.

[25] A. Bauereiß, T. Scharowsky, and C. Körner, "Defect generation and propagation mechanism during additive manufacturing by selective beam melting," J. Mater. Process. Technol., vol. 214, no. 11, pp. 2522–2528, Nov. 2014, doi: 10.1016/J.JMATPROTEC.2014.05.002.

[26] R. Li, Y. Shi, Z. Wang, L. Wang, J. Liu, and W. Jiang, "Densification behavior of gas and water atomized 316L stainless steel powder during selective laser melting," Appl. Surf. Sci., 2010, doi: 10.1016/j.apsusc.2010.02.030.

[27] E. Brandl, Microstructural and mechanical properties of additive manufactured titanium (Ti-6Al-4V) using wire Evaluation with respect to additive processes using powder and aerospace material specifications. 2010.

[28] K. Puebla, L. E. Murr, S. M. Gaytan, E. Martinez, F. Medina, and R. B. Wicker, “Effect of Melt Scan Rate on Microstructure and Macrostructure for Electron Beam Melting of Ti-6Al-4V,” Mater. Sci. Appl., vol. 03, no. 05, pp. 259–264, May 2012, doi: 10.4236/msa.2012.35038.

[29] G. Miranda et al., “Predictive models for physical and mechanical properties of 316L stainless steel produced by selective laser melting,” Mater. Sci. Eng. A, vol. 657, pp. 43–56, 2016, doi: 10.1016/j.msea.2016.01.028.

[30] P. . Kobryn and S. . Semiatin, “Microstructure and texture evolution during solidification processing of Ti–6Al–4V,” J. Mater. Process. Technol., vol. 135, no. 2–3, pp. 330–339, Apr. 2003, doi: 10.1016/S0924-0136(02)00865-8.

[31] R. Cottam and M. Brandt, “Laser Cladding of Ti-6Al-4 V Powder on Ti-6Al-4 V Substrate: Effect of Laser Cladding Parameters on Microstructure,” Phys. Procedia, vol. 12, pp. 323–329, Jan. 2011, doi: 10.1016/J.PHPRO.2011.03.041.

[32] L. Li, “Repair of directionally solidified superalloy GTD-111 by laser-engineered net shaping,” J. Mater. Sci., 2006, doi: 10.1007/s10853-006-0948-0.

[33] W. E. King et al., “Observation of keyhole-mode laser melting in laser powder-bed fusion additive manufacturing,” J. Mater. Process. Technol., vol. 214, no. 12, pp. 2915–2925, 2014, doi: 10.1016/j.jmatprotec.2014.06.005.

[34] H. Gong, K. Rafi, N. V. Karthik, T. Starr, and B. Stucker, “Defect morphology in Ti-6Al-4V parts fabricated by Selective Laser Melting and Electron Beam Melting,” 24th Int. SFF Symp. - An Addit. Manuf. Conf. SFF 2013, no. July 2015, pp. 440–453, 2013, doi: 10.1007/s11665-013-0658-0.

[35] W. E. King, A. T. Anderson, R. M. Ferencz, N. E. Hodge, C. Kamath, and S. A. Khairallah, “MODELING AND SIMULATION OF ADDITIVE MANUFACTURING PROCESSES.” Accessed: Sep. 30, 2018. [Online]. Available: http://www.aspe.net/publications/Short Abstracts 14SP/3990.pdf.

[36] P. Yuan and D. Gu, “Molten pool behaviour and its physical mechanism during

selective laser melting of TiC/AlSi10Mg nanocomposites: Simulation and experiments," J. Phys. D. Appl. Phys., vol. 48, no. 3, 2015, doi: 10.1088/0022-3727/48/3/035303.

[37] J.-H. Cho and S.-J. Na, "Implementation of real-time multiple reflection and Fresnel absorption of laser beam in keyhole," J. Phys. D. Appl. Phys., vol. 39, no. 24, pp. 5372–5378, Dec. 2006, doi: 10.1088/0022-3727/39/24/039.

[38] R. Rai, P. Burgardt, J. O. Milewski, T. J. Lienert, and T. DebRoy, "Heat transfer and fluid flow during electron beam welding of 21Cr–6Ni–9Mn steel and Ti–6Al–4V alloy," J. Phys. D. Appl. Phys., vol. 42, no. 2, p. 025503, Jan. 2009, doi: 10.1088/0022-3727/42/2/025503.

[39] S. Pang, W. Chen, and W. Wang, "A quantitative model of keyhole instability induced porosity in laser welding of titanium alloy," Metall. Mater. Trans. A Phys. Metall. Mater. Sci., 2014, doi: 10.1007/s11661-014-2231-3.

[40] V. Semak and A. Matsunawa, "The role of recoil pressure in energy balance during laser materials processing," J. Phys. D. Appl. Phys., vol. 30, no. 18, pp. 2541–2552, Sep. 1997, doi: 10.1088/0022-3727/30/18/008.

[41] S. . Tsirkas, P. Papanikos, and T. Kermanidis, "Numerical simulation of the laser welding process in butt-joint specimens," J. Mater. Process. Technol., vol. 134, no. 1, pp. 59–69, Mar. 2003, doi: 10.1016/S0924-0136(02)00921-4.

[42] D. Dai and D. Gu, "Thermal behavior and densification mechanism during selective laser melting of copper matrix composites: Simulation and experiments," Mater. Des., vol. 55, pp. 482–491, Mar. 2014, doi: 10.1016/J.MATDES.2013.10.006.

[43] L. Thijs, K. Kempen, J.-P. P. Kruth, and J. Van Humbeeck, "Fine-structured aluminium products with controllable texture by selective laser melting of pre-alloyed AlSi10Mg powder," Acta Mater., vol. 61, no. 5, pp. 1809–1819, Mar. 2013, doi: 10.1016/j.actamat.2012.11.052.

[44] Y. Liu, Y. Yang, S. Mai, D. Wang, and C. Song, "Investigation into spatter behavior

during selective laser melting of AISI 316L stainless steel powder," Mater. Des., vol. 87, pp. 797–806, Dec. 2015, doi: 10.1016/J.MATDES.2015.08.086.

[45] M. Geiger, K.-H. Leitz, H. Koch, and A. Otto, "A 3D transient model of keyhole and melt pool dynamics in laser beam welding applied to the joining of zinc coated sheets," Prod. Eng., vol. 3, no. 2, pp. 127–136, Jun. 2009, doi: 10.1007/s11740-008-0148-7.

[46] H. Attar, M. Calin, L. C. C. Zhang, S. Scudino, and J. Eckert, "Manufacture by selective laser melting and mechanical behavior of commercially pure titanium," Mater. Sci. Eng. A, vol. 593, pp. 170–177, Jan. 2014, doi: 10.1016/j.msea.2013.11.038.

[47] S. I. Anisimov and V. A. Khokhlov, Instabilities in Laser-matter interaction. CRC Press, 1995.

[48] J.R. Davis & Associates. and ASM International., ASM materials engineering dictionary. ASM International, 1992.

[49] W. Xu et al., "Additive manufacturing of strong and ductile Ti-6Al-4V by selective laser melting via in situ martensite decomposition," Acta Mater., vol. 85, pp. 74–84, 2015, doi: 10.1016/j.actamat.2014.11.028.

[50] M. Simonelli, Y. Y. Tse, and C. Tuck, "Effect of the build orientation on the mechanical properties and fracture modes of SLM Ti-6Al-4V," Mater. Sci. Eng. A, vol. 616, pp. 1–11, 2014, doi: 10.1016/j.msea.2014.07.086.

[51] P. Edwards and M. Ramulu, "Fatigue performance evaluation of selective laser melted Ti-6Al-4V," Mater. Sci. Eng. A, vol. 598, pp. 327–337, 2014, doi: 10.1016/j.msea.2014.01.041.

[52] J. L. Gilbert and H. R. Piehler, "On the nature and crystallographic orientation of subsurface cracks in high cycle fatigue of Ti-6Al-4V," Metall. Trans. A, vol. 24, no. 3, pp. 669–680, Mar. 1993, doi: 10.1007/BF02656635.

[53] K. Rekedal and D. Liu, "Fatigue Life of Selective Laser Melted and Hot Isostatically

Pressed Ti-6Al-4v Absent of Surface Machining," Jan. 2015, doi: 10.2514/6.2015-0894.

[54] E. Wycisk, C. Emmelmann, S. Siddique, and F. Walther, "High Cycle Fatigue (HCF) Performance of Ti-6Al-4V Alloy Processed by Selective Laser Melting," Adv. Mater. Res., vol. 816–817, pp. 134–139, Sep. 2013, doi: 10.4028/www.scientific.net/AMR.816-817.134.

[55] H. K. Rafi, T. L. Starr, and B. E. Stucker, "A comparison of the tensile, fatigue, and fracture behavior of Ti–6Al–4V and 15-5 PH stainless steel parts made by selective laser melting," Int. J. Adv. Manuf. Technol., vol. 69, no. 5–8, pp. 1299–1309, Nov. 2013, doi: 10.1007/s00170-013-5106-7.

[56] G. Kasperovich and J. Hausmann, "Improvement of fatigue resistance and ductility of TiAl6V4 processed by selective laser melting," J. Mater. Process. Technol., vol. 220, pp. 202–214, Jun. 2015, doi: 10.1016/j.jmatprotec.2015.01.025.

[57] S. Leuders, A. Riemer, and H. A. Richard, "Influence of heat-treatment on Selective Laser Melting products – e.g. Ti6Al4V," 2015. Accessed: Sep. 30, 2018. [Online]. Available: https://www.researchgate.net/publication/267422255.

[58] S. Leuders et al., "On the mechanical behaviour of titanium alloy TiAl6V4 manufactured by selective laser melting: Fatigue resistance and crack growth performance," Int. J. Fatigue, vol. 48, pp. 300–307, 2013, doi: 10.1016/j.ijfatigue.2012.11.011.

[59] M. Shiomi, K. Osakada, K. Nakamura, T. Yamashita, and F. Abe, "Residual Stress within Metallic Model Made by Selective Laser Melting Process," CIRP Ann., vol. 53, no. 1, pp. 195–198, Jan. 2004, doi: 10.1016/S0007-8506(07)60677-5.

[60] C.-W. Lin, C.-P. Ju, and J.-H. Chern Lin, "A comparison of the fatigue behavior of cast Ti–7.5Mo with c.p. titanium, Ti–6Al–4V and Ti–13Nb–13Zr alloys," Biomaterials, vol. 26, no. 16, pp. 2899–2907, Jun. 2005, doi: 10.1016/J.BIOMATERIALS.2004.09.007.

[61] N. Hrabe and T. Quinn, “Effects of processing on microstructure and mechanical properties of a titanium alloy (Ti–6Al–4V) fabricated using electron beam melting (EBM), part 1: Distance from build plate and part size,” Mater. Sci. Eng. A, vol. 573, pp. 264–270, Jun. 2013, doi: 10.1016/J.MSEA.2013.02.064.

[62] R. K. Nalla, R. O. Ritchie, B. L. Boyce, J. P. Campbell, and J. O. Peters, “Influence of microstructure on high-cycle fatigue of Ti-6Al-4V: Bimodal vs. lamellar structures,” Metall. Mater. Trans. A, vol. 33, no. 3, pp. 899–918, Mar. 2002, doi: 10.1007/s11661-002-0160-z.

[63] G. Nicoletto, “Anisotropic high cycle fatigue behavior of Ti–6Al–4V obtained by powder bed laser fusion,” Int. J. Fatigue, vol. 94, pp. 255–262, 2017, doi: 10.1016/j.ijfatigue.2016.04.032.

[64] S. Leuders, M. Vollmer, F. Brenne, T. Tröster, and T. Niendorf, “Fatigue Strength Prediction for Titanium Alloy TiAl6V4 Manufactured by Selective Laser Melting,” Metall. Mater. Trans. A, vol. 46, no. 9, pp. 3816–3823, Sep. 2015, doi: 10.1007/s11661-015-2864-x.

[65] D. Li, L. Q. Liang, and W. J. Zhang, “Defect inspection and extraction of the mobile phone cover glass based on the principal components analysis,” Int. J. Adv. Manuf. Technol., 2014, doi: 10.1007/s00170-014-5871-y.

[66] J. Risse, C. Golebiewski, W. Meiners, and K. Wissenbach, Fachmesse und Anwendert agung für apid-Technologie agungsband 013. rfurt: ESOTRON, 013.

[67] M. Geiger, International Institution for Production Engineering Research, and 1994 LANE <1, Laser assisted net shape engineering proceedings of the 26th International CIRP Seminar on Manufacturing Systems - LANE ’94, Erlangen, October 12-14, 1994. Meisenbach, 1994.

[68] Y. Liu, Y. Yang, S. Mai, D. Wang, and C. Song, “Investigation into spatter behavior during selective laser melting of AISI 316L stainless steel powder,” 2015, doi: 10.1016/j.matdes.2015.08.086.

[69] H. J. Niu and I. T. H. Chang, “LIQUID PHASE SINTERING OF M3/2 HIGH SPEED STEEL BY SELECTIVE LASER SINTERING,” 1998. Accessed: Sep. 30, 2018. [Online]. Available: https://ac.els-cdn.com/S1359646298001262/1-s2.0-S1359646298001262-main.pdf?_tid=f832b4d6-cfc1-484d-8ff0-8505efabc78f&acdnat=1538331594_8daa290e0eaf8d5da332d6e18c2d883b.

[70] D. Gu and Y. Shen, “Balling phenomena in direct laser sintering of stainless steel powder: Metallurgical mechanisms and control methods,” Mater. Des., 2009, doi: 10.1016/j.matdes.2009.01.013.

[71] J. Choi and Y. Chang, “Characteristics of laser aided direct metal/material deposition process for tool steel,” Int. J. Mach. Tools Manuf., vol. 45, no. 4–5, pp. 597–607, Apr. 2005, doi: 10.1016/J.IJMACHTOOLS.2004.08.014.

[72] G. K. Lewis and E. Schlienger, “Practical considerations and capabilities for laser assisted direct metal deposition,” Mater. Des., vol. 21, no. 4, pp. 417–423, Aug. 2000, doi: 10.1016/S0261-3069(99)00078-3.

[73] A. Simchi and H. Pohl, “Effects of laser sintering processing parameters on the microstructure and densification of iron powder,” Mater. Sci. Eng. A, 2003, doi: 10.1016/S0921-5093(03)00341-1.

[74] B. J. Keene, “Review of data for the surface tension of iron and its binary alloys,” Int. Mater. Rev., vol. 33, no. 1, pp. 1–37, Jan. 1988, doi: 10.1179/imr.1988.33.1.1.

[75] R. Li, J. Liu, Y. Shi, L. Wang, and W. Jiang, “Balling behavior of stainless steel and nickel powder during selective laser melting process,” Int. J. Adv. Manuf. Technol., vol. 59, no. 9–12, pp. 1025–1035, 2012, doi: 10.1007/s00170-011-3566-1.

[76] G. Kasperovich, J. Haubrich, J. Gussone, and G. Requena, “Correlating between porosity and processing parameters in Ti-6Al-4V produced by selective laser melting,” Mater. Des., vol. 105, pp. 160–170, 2016.

[77] X. Zhou, X. Liu, D. Zhang, Z. Shen, and W. Liu, “Balling phenomena in selective

laser melted tungsten," J. Mater. Process. Technol., vol. 222, pp. 33–42, Aug. 2015, doi: 10.1016/J.JMATPROTEC.2015.02.032.

[78] X. Zhou et al., "3D-imaging of selective laser melting defects in a Co-Cr-Mo alloy by synchrotron radiation micro-CT," Acta Mater., vol. 98, pp. 1–16, 2015, doi: 10.1016/j.actamat.2015.07.014.

[79] B. K. Foster, E. W. Reutzel, A. R. Nassar, B. T. Hall, S. W. Brown, and C. J. Dickman, "Optical, layerwise monitoring of powder bed fusion." Accessed: Oct. 01, 2018. [Online]. Available: https://sffsymposium.engr.utexas.edu/sites/default/files/2015/2015-24-Foster.pdf.

[80] S. J. Foster et al., "Process-Defect-Structure-Property Correlations During Laser Powder Bed Fusion of Alloy 718: Role of In Situ and Ex Situ Characterizations," Metall. Mater. Trans. A Phys. Metall. Mater. Sci., vol. 49, no. 11, pp. 5775–5798, 2018, doi: 10.1007/s11661-018-4870-2.

[81] S. V. Alekseenko and V. E. Nakoryakov, "Instability of a liquid film moving under the effect of gravity and gas flow," Int. J. Heat Mass Transf., vol. 38, no. 11, pp. 2127–2134, Jul. 1995, doi: 10.1016/0017-9310(94)00326-Q.

[82] Y. Y. Trifonov, "Wave formation in a film Flowing down an inclined plane in the presence of phase change and tangential tension on a free surface," J. Appl. Mech. Tech. Phys., vol. 37, no. 2, pp. 241–249, Mar. 1996, doi: 10.1007/BF02382431.

[83] H. A. Stoffregen, K. Butterweck, and E. Abele, "Fatigue Analysis in Selective Laser Melting: Review and Investigation of Thin-Walled Actuator Housings," 2014.

[84] Z. Liu, S. L. Lu, H. P. Tang, M. Qian, and L. Zhan, "Characterization and decompositional crystallography of the massive phase grains in an additively-manufactured Ti-6Al-4V alloy," Mater. Charact., vol. 127, pp. 146–152, 2017, doi: 10.1016/j.matchar.2017.01.012.

[85] Y. Chivel and I. Smurov, "On-line temperature monitoring in selective laser sintering/melting," in Physics Procedia, Jan. 2010, vol. 5, no. PART 2, pp. 515–521,

doi: 10.1016/j.phpro.2010.08.079.

[86] Y. Chivel, “Optical in-process temperature monitoring of selective laser melting,” in Physics Procedia, Jan. 2013, vol. 41, pp. 904–910, doi: 10.1016/j.phpro.2013.03.165.

[87] P. Lott, H. Schleifenbaum, W. Meiners, K. Wissenbach, C. Hinke, and J. Bültmann, “Design of an optical system for the in situ process monitoring of Selective Laser Melting (SLM),” Phys. Procedia, vol. 12, no. PART 1, pp. 683–690, 2011, doi: 10.1016/j.phpro.2011.03.085.

[88] M. Grasso, V. Laguzza, Q. Semeraro, and B. M. Colosimo, “In-Process Monitoring of Selective Laser Melting: Spatial Detection of Defects Via Image Data Analysis,” J. Manuf. Sci. Eng., 2016, doi: 10.1115/1.4034715.

[89] M. Grasso and B. M. Colosimo, “Process defects and in situ monitoring methods in metal powder bed fusion: A review,” Meas. Sci. Technol., vol. 28, no. 4, 2017, doi: 10.1088/1361-6501/aa5c4f.

[90] H. Krauss, T. Zeugner, and M. F. Zaeh, “Layerwise monitoring of the Selective Laser Melting process by thermography,” in Physics Procedia, Jan. 2014, vol. 56, no. C, pp. 64–71, doi: 10.1016/j.phpro.2014.08.097.

[91] G. Repossini, V. Laguzza, M. Grasso, and B. M. Colosimo, “On the use of spatter signature for in-situ monitoring of Laser Powder Bed Fusion,” Addit. Manuf., 2017, doi: 10.1016/j.addma.2017.05.004.

[92] K. Zhang, T. Liu, W. Liao, C. Zhang, D. Du, and Y. Zheng, “Photodiode data collection and processing of molten pool of alumina parts produced through selective laser melting,” Optik (Stuttg)., vol. 156, pp. 487–497, Mar. 2018, doi: 10.1016/j.ijleo.2017.11.143.

[93] S. Van Bael, G. Kerckhofs, M. Moesen, G. Pyka, J. Schrooten, and J. P. Kruth, “Micro-CT-based improvement of geometrical and mechanical controllability of selective laser melted Ti6Al4V porous structures,” Mater. Sci. Eng. A, vol. 528, no. 24, pp. 7423–7431, Sep. 2011, doi: 10.1016/j.msea.2011.06.045.

[94] A. Bobel et al., “In situ synchrotron X-ray imaging of 4140 steel laser powder bed fusion,” Materialia, vol. 6, p. 100306, Jun. 2019, doi: 10.1016/j.mtla.2019.100306.

[95] T. Grimm, G. Wiora, and G. Witt, “Characterization of typical surface effects in additive manufacturing with confocal microscopy,” Surf. Topogr. Metrol. Prop., 2015, doi: 10.1088/2051-672X/3/1/014001.

[96] J. C. Fox, S. P. Moylan, and B. M. Lane, “Effect of Process Parameters on the Surface Roughness of Overhanging Structures in Laser Powder Bed Fusion Additive Manufacturing,” in Procedia CIRP, Jan. 2016, vol. 45, pp. 131–134, doi: 10.1016/j.procir.2016.02.347.

[97] C. Gomez, R. Su, A. Thompson, J. DiSciacca, S. Lawes, and R. Leach, “Optimization of surface measurement for metal additive manufacturing using coherence scanning interferometry,” Opt. Eng., vol. 56, no. 11, p. 111714, Jul. 2017, doi: 10.1117/1.OE.56.11.111714.

[98] A. T. Sidambe, “Three dimensional surface topography characterization of the electron beam melted Ti6Al4V,” Met. Powder Rep., vol. 72, no. 3, pp. 200–205, May 2017, doi: 10.1016/j.mprp.2017.02.003.

[99] A. Townsend, R. Racasan, and L. Blunt, “Surface-specific additive manufacturing test artefacts,” Surf. Topogr. Metrol. Prop., vol. 6, no. 2, p. 024007, May 2018, doi: 10.1088/2051-672X/aabcaf.

[100] A. Triantaphyllou et al., “Surface texture measurement for additive manufacturing,” Surf. Topogr. Metrol. Prop., 2015, doi: 10.1088/2051-672X/3/2/024002.

[101] F. Cabanettes et al., “Topography of as built surfaces generated in metal additive manufacturing: A multi scale analysis from form to roughness,” Precis. Eng., vol. 52, pp. 249–265, Apr. 2018, doi: 10.1016/j.precisioneng.2018.01.002.

[102] W. S. Gora et al., “Enhancing surface finish of additively manufactured titanium and cobalt chrome elements using laser based finishing,” in Physics Procedia, Jan. 2016, vol. 83, pp. 258–263, doi: 10.1016/j.phpro.2016.08.021.

[103] Y. Y. Sun et al., “The Influence of As-Built Surface Conditions on Mechanical Properties of Ti-6Al-4V Additively Manufactured by Selective Electron Beam Melting,” JOM, vol. 68, no. 3, pp. 791–798, Mar. 2016, doi: 10.1007/s11837-015-1768-y.

[104] B. Rosa, P. Mognol, and J. Hascoët, “Laser polishing of additive laser manufacturing surfaces,” J. Laser Appl., vol. 27, no. S2, p. S29102, Feb. 2015, doi: 10.2351/1.4906385.

[105] A. G. Demir and B. Previtali, “Additive manufacturing of cardiovascular CoCr stents by selective laser melting,” Mater. Des., vol. 119, pp. 338–350, Apr. 2017, doi: 10.1016/j.matdes.2017.01.091.

[106] A. Thompson, N. Senin, C. Giusca, and R. Leach, “Topography of selectively laser melted surfaces: A comparison of different measurement methods,” CIRP Ann. - Manuf. Technol., vol. 66, no. 1, pp. 543–546, Jan. 2017, doi: 10.1016/j.cirp.2017.04.075.

[107] M. Aminzadeh and T. R. Kurfess, “Online quality inspection using Bayesian classification in powder-bed additive manufacturing from high-resolution visual camera images,” J. Intell. Manuf., vol. 30, no. 6, pp. 2505–2523, Aug. 2019, doi: 10.1007/s10845-018-1412-0.

[108] L. Scime and J. Beuth, “Anomaly detection and classification in a laser powder bed additive manufacturing process using a trained computer vision algorithm,” Addit. Manuf., vol. 19, pp. 114–126, Jan. 2018, doi: 10.1016/j.addma.2017.11.009.

[109] L. Scime and J. Beuth, “A multi-scale convolutional neural network for autonomous anomaly detection and classification in a laser powder bed fusion additive manufacturing process,” Addit. Manuf., vol. 24, no. October, pp. 273–286, 2018, doi: 10.1016/j.addma.2018.09.034.

[110] Y. Zhang, G. S. Hong, D. Ye, K. Zhu, and J. Y. H. Fuh, “Extraction and evaluation of melt pool, plume and spatter information for powder-bed fusion AM process

monitoring," Mater. Des., vol. 156, pp. 458–469, Oct. 2018, doi: 10.1016/j.matdes.2018.07.002.

[111] M. Grasso, F. Gallina, and B. M. Colosimo, "Data fusion methods for statistical process monitoring and quality characterization in metal additive manufacturing," in Procedia CIRP, Jan. 2018, vol. 75, pp. 103–107, doi: 10.1016/j.procir.2018.04.045.

[112] P. K. Rao, J. Liu, D. Roberson, Z. Kong, and C. Williams, "Online Real-Time Quality Monitoring in Additive Manufacturing Processes Using Heterogeneous Sensors," J. Manuf. Sci. Eng. Trans. ASME, vol. 137, no. 6, Dec. 2015, doi: 10.1115/1.4029823.

[113] J. Petrich, C. Gobert, S. Phoha, A. R. Nassar, and E. W. Reutzel, "Machine learning for defect detection for PBFAm using high resolution layerwise imaging coupled with post-build CT scans." 2020, Accessed: Apr. 01, 2021. [Online]. Available: https://pennstate.pure.elsevier.com/en/publications/machine-learning-for-defect-detection-for-pbfam-using-high-resolu.

[114] C. Gobert, E. W. Reutzel, J. Petrich, A. R. Nassar, and S. Phoha, "Application of supervised machine learning for defect detection during metallic powder bed fusion additive manufacturing using high resolution imaging.," Addit. Manuf., vol. 21, no. April, pp. 517–528, 2018, doi: 10.1016/j.addma.2018.04.005.

[115] M. S. Tootooni, A. Dsouza, R. Donovan, P. K. Rao, Z. J. Kong, and P. Borgesen, "Classifying the Dimensional Variation in Additive Manufactured Parts from Laser-Scanned Three-Dimensional Point Cloud Data Using Machine Learning Approaches," J. Manuf. Sci. Eng. Trans. ASME, vol. 139, no. 9, Sep. 2017, doi: 10.1115/1.4036641.

[116] J. (Peter) Liu, C. Liu, Y. Bai, P. Rao, C. B. Williams, and Z. (James) Kong, "Layer-wise spatial modeling of porosity in additive manufacturing," IISE Trans., vol. 51, no. 2, pp. 109–123, Feb. 2019, doi: 10.1080/24725854.2018.1478169.

[117] N. Senin and R. Leach, "Information-rich surface metrology," in Procedia CIRP, Jan. 2018, vol. 75, pp. 19–26, doi: 10.1016/j.procir.2018.05.003.

[118] W. P. Syam, K. Rybalcenko, A. Gaio, J. Crabtree, and R. K. Leach, “Methodology for the development of in-line optical surface measuring instruments with a case study for additive surface finishing,” Opt. Lasers Eng., vol. 121, pp. 271–288, Oct. 2019, doi: 10.1016/j.optlaseng.2019.04.015.

[119] D. Weimer, B. Scholz-Reiter, and M. Shpitalni, “Design of deep convolutional neural network architectures for automated feature extraction in industrial inspection,” CIRP Ann. - Manuf. Technol., 2016, doi: 10.1016/j.cirp.2016.04.072.

[120] D. H. Hubel and T. N. Wiesel, “Receptive fields, binocular interaction and functional architecture in the cat’s visual cortex,” J. Physiol., 1962, doi: 10.1113/jphysiol.1962.sp006837.

[121] A. G. Howard et al., “MobileNets: Efficient Convolutional Neural Networks for Mobile Vision Applications,” arXiv, Apr. 2017, Accessed: Apr. 01, 2021. [Online]. Available: http://arxiv.org/abs/1704.04861.

[122] Y. Lecun, Y. Bengio, and G. Hinton, “Deep learning,” Nature, vol. 521, no. 7553. Nature Publishing Group, pp. 436–444, May 27, 2015, doi: 10.1038/nature14539.

[123] V. Nair and G. E. Hinton, “Rectified Linear Units Improve Restricted Boltzmann Machines,” Jan. 2010.

[124] R. M. Neal, “Pattern Recognition and Machine Learning,” Technometrics, 2007, doi: 10.1198/tech.2007.s518.

[125] P. V. Ca, L. T. Edu, I. Lajoie, Y. B. Ca, and P.-A. M. Ca, “Stacked Denoising Autoencoders: Learning Useful Representations in a Deep Network with a Local Denoising Criterion Pascal Vincent Hugo Larochelle Yoshua Bengio Pierre-Antoine Manzagol,” 2010.

[126] R. Hecht-Nielsen, “Theory of the backpropagation neural network,” 1989, pp. 593–605, doi: 10.1109/ijcnn.1989.118638.

[127] O. Ronneberger, P. Fischer, and T. Brox, “U-Net: Convolutional Networks for

Biomedical Image Segmentation.” Accessed: Apr. 01, 2021. [Online]. Available: http://lmb.informatik.uni-freiburg.de/.